Universidade Federal de São Carlos
Centro de Ciências Exatas e de Tecnologia
Programa de Pós-Graduação em Engenharia Elétrica

Raphael Pinto Ferreira

Estimating sugarcane rows orientation in aerial images

São Carlos - SP
2022

Raphael Pinto Ferreira

Estimating sugarcane rows orientation in aerial images

Dissertação apresentada ao Programa de Pós-Graduação em Engenharia Elétrica do Centro de Ciências Exatas e de Tecnologia da Universidade Federal de São Carlos, como parte dos requisitos para a obtenção do título de Mestre em Engenharia Elétrica.

Área de concentração: Sistemas Elétricos e Eletrônicos

Supervisor: Prof. Dr. André Carmona Hernandes

São Carlos - SP
2022

UNIVERSIDADE FEDERAL DE SÃO CARLOS

Centro de Ciências Exatas e de Tecnologia
Programa de Pós-Graduação em Engenharia Elétrica

Folha de Aprovação

Defesa de Dissertação de Mestrado do candidato Raphael Pinto Ferreira, realizada em 13/12/2022.

Comissão Julgadora:

Prof. Dr. Andre Carmona Hernandes (UFSCar)

Prof. Dr. Marcelo Becker (USP)

Prof. Dr. Jones Yudi Mori Alves da Silva (UnB)

O Relatório de Defesa assinado pelos membros da Comissão Julgadora encontra-se arquivado junto ao Programa de Pós-Graduação em Engenharia Elétrica.

Acknowledgements

I thank God, who, in addition to allowing all of this work to happen, also gave me the strength and wisdom to get here. To all my family, especially my wife Karen, for encouraging my studies and always rooting for my success. To my advisor, Dr. André Carmona Hernandes, for his guidance, patience and trust with me. To Dr. Marcelo Becker and Dr. Jones Yudi for all advice and contributions to this work. To the professors and employees of the Department of Electrical Engineering (DEE) of the Federal University of São Carlos (UFSCar) for the disciplines taught and for all the necessary support during this period. To my postgraduate colleagues and to the *Mobile Robotics Laboratory* Group, for the exchange of ideas, help and friendship.

"Porque dele e por ele, e para ele,
são todas as coisas; glória pois a ele eternamente. Amém."
Romanos 12:36

Abstract

With the growth of the world population, the demand for agricultural areas has reached the limits of sustainability. It is then urgent to increase the efficiency of plantations, producing a more significant amount of crop without increasing the planted areas. In this context, the area of Precision Farming has emerged, integrating state-of-the-art technologies into agricultural systems. One of the most demanded cultivars is sugarcane, used both as food and biofuel. In sugarcane harvesting, the precision of a few centimetres is required to prevent the cultivars from being crushed by the harvesters. The autonomous harvesters are guided by satellite positioning systems, whose precision can reach several meters. One proposed solution is to use unmanned aerial vehicles equipped with cameras and other sensors capable of providing real-time information to the harvesters. This work shows the development of image analysis for estimating crop orientation by two heuristic approach using some well-know processing techniques. To validate the solution architecture, an aerial image set was acquired and labeled by experts. To create a robust ground truth, a methodology for fusion of experts voting was used. With the ground truth, the estimating technique was validated, and its implementation was analysed, presenting performance and quality within the application requirements.

Keywords: Remore Sensing, Crop-row, Sugarcane, Radon Transform, Savitzky-Golay.

Resumo

Com o crescimento da população mundial, a demanda por áreas agrícolas atingiu os limites da sustentabilidade. Por isso há urgência em aumentar a eficiência das plantações, produzindo uma quantidade de colheita mais significativa sem aumentar as áreas plantadas. Nesse contexto, surgiu o campo da Agricultura de Precisão, integrando tecnologias de ponta aos sistemas agrícolas. Uma das cultivares mais demandadas é a cana-de-açúcar, utilizada tanto como alimento quanto como biocombustível. Na colheita da cana-de-açúcar, é necessária uma precisão de alguns centímetros para evitar que as cultivares sejam esmagadas pelas colhedoras. As colheitadeiras autônomas são guiadas por sistemas de posicionamento por satélite, cuja precisão pode chegar a vários metros. Uma solução proposta é a utilização de veículos aéreos não tripulados equipados com câmeras e outros sensores capazes de fornecer informações em tempo real aos colhedores. Este trabalho mostra o desenvolvimento da análise de imagem para estimar a orientação da cultura por duas abordagens heurísticas usando algumas técnicas de processamento bem conhecidas. Para validar a arquitetura da solução, um conjunto de imagens aéreas foi adquirido e rotulado por especialistas. Para criar uma comparação robusta, uma metodologia de fusão de votos de especialistas foi usada. Com a verdade absoluta mensurada, a técnica de estimação do ângulo de cultivo foi validada e sua implementação foi analisada, apresentando desempenho e qualidade dentro dos requisitos da aplicação.

Palavras-chave: Sensoriamento Remoto, Linha de colheita, Cana-de-açucar, Transformada Radon, Savitzky-Golay.

List of Figures

List of Tables

Lista de siglas

CCD *Charge Coupled Device*

CEPEA Centro de Estudos Avançados em Econômia Aplicada

CMOS *Complementary Metal Oxide Semiconductor*

DECEA Departamento de Controle do Espaço Aéreo

UAV *Unmanned Aerial Vehicle*

VLOS Visual Line of Sight

Contents

Chapter 1

Introduction

The recent trajectory of Brazilian agriculture is the result of a combination of factors. Among these factors, what made the most difference in the last 50 years were investments in agricultural research. Advances in science, appropriate technologies and innovations can be called agricultural investment (EMBRAPA, 2018). As can be seen in figure 1, the planted area did not follow the growth of production, this is due to the lack of land for the horizontal growth of agriculture in Brazil and in the world. In other words, there are strong reasons for increasing agricultural production to occur through the intensification of production systems and not by increasing the area used for growing plants and raising animals (EMBRAPA, 2018). The recent modernization of Brazilian agriculture is the main contributor to an intensification of agricultural production without the need for territorial expansion.

Figure 1 – Production indicators and planted area from 1975 to 2017.

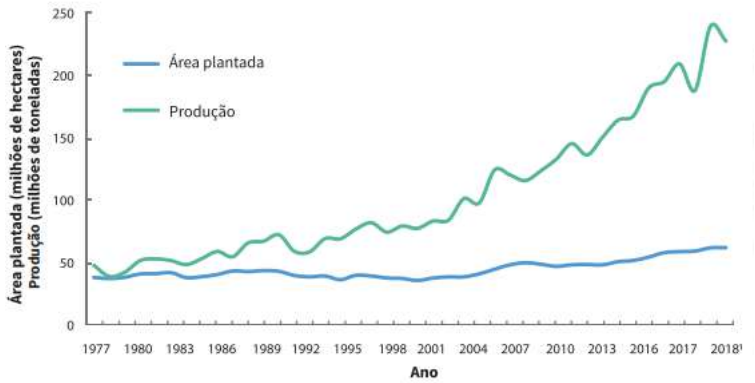

Source: (EMBRAPA, 2018)

With these technological advances, precision agriculture (PA) emerged. Precision

agriculture can be understood as a set of tools and technologies that allows the producer to know the entire area for cultivation in a more complete way and work more efficiently. Precision farming is a holistic and innovative systems approach that assists farmers in managing crop and soil variability in order to lower costs, improve yield quality and quantity, and increase farm income (PAUSTIAN; THEUVSEN, 2017), reducing the use of chemicals to prevent environmental damage and produce high quality products to satisfy the growing demand for food (MOURHIR et al., 2017) (ONYANGO et al., 2021). PA applies traditional agricultural practices with new technologies, practices and economic drivers to increase sustainability in a dynamic balance (BALAFOUTIS et al., 2017).

The use of Unmanned Aerial Vehicles (UAVs) for remote sensing offers the possibility of acquiring field data in an easy, fast and economical way compared to the methods mentioned above. The constant evolution of cameras to obtain better image resolution, together with the fact that UAVs fly at low altitudes, also contributes to better resolutions in the images obtained, in addition to the high temporal resolution. Furthermore, UAVs are much simpler to use and also cheaper than manned aircraft. Its use is also more efficient than terrestrial systems, as they promote a field sweep in a short time (TSOUROS; BIBI; SARIGIANNIDIS, 2019). Unmanned Aerial Systems (UAS) are now used in remote sensing applications for Precision Agriculture, serving a multitude of purposes such as, for example, health monitoring and disease detection, growth monitoring and yield estimation, weed management and detection, among others. (ZHANG; KOVACS, 2012) (PURI; NAYYAR; RAJA, 2017) (MOGILI; DEEPAK, 2018) (YANG et al., 2017) (KULBACKI et al., 2018).

1.1 Motivation

The concept of linear rows planting is considered a very attractive approach for most of cultures and farmers. The main advantages is related to maximizing the light exposure for the plants, providing wind passage along the inter-rows to enhance the gas exchange, enhancing the movement between plants especially for planting, weeding, pest control and harvesting operations.

In the recent years, harvesting mechanization experimented huge technological advances that is related with the increase production of sugarcane which is one of the most planted crops on the planet (CONAB, 2021). The mechanization of harvesting relies on satellite-based positioning, navigation and timing (PNT) systems, also known as Global Navigation Satellite System (GNSS). However, location accuracy depends on the technology used, position errors can range from 9 m to 2.5 cm (KRüGER; SPRINGER; LECHNER, 1994). Therefore, in agricultural applications, correction systems must be integrated with GNSS to achieve the highest accuracy, in centimeter order (CELADES-MARTíNEZ et al., 2020).

The GNSS-RTK is one of these correction system that provides geographic accuracy, which has the potential to optimize cropping patterns in agricultural fields. This technology uses an RTK base that remains in a fixed position and processes the position of the GNSS signal for a long time to enable the high accuracy of its location. Once this is done, RTK can reliably compare your current position with the actual GNSS signal to determine what the current error of the GNSS signal is. Then RTK sends this error signal to the harvester which receives it and applies the GNSS coordinate compensation, see figure 2.

One of the disadvantages is that the base signal must reach the harvester via radio frequency waves. The maximum distance between them can be up to 60 km and natural or artificial obstacles can interrupt the transmission. In these situations, the autopilot of the agricultural machine loses the accuracy of the crop line, causing the harvester to pass over the crop or enter a collision course with the transhipment tractor. Therefore, an alternative to traditional satellite navigation systems for sugarcane harvesters is needed.

Figure 2 – Representation of the use of the GNSS-RTK system in the harvest..

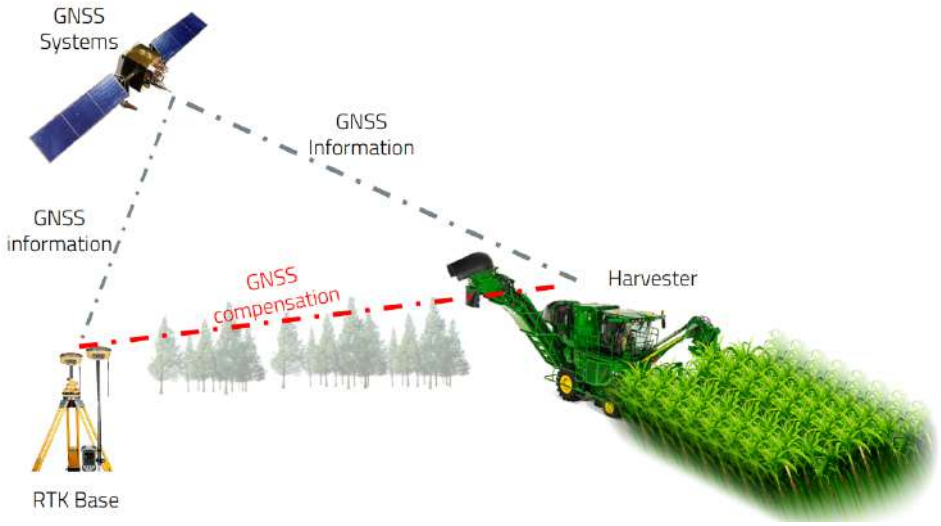

Source: Author.

1.2 Problem Description

The main goal of this work is the development of a heuristic that allows UAV to identify the direction of the sugarcane plantation lines to help harvesters in their trajectories in the future, as illustrated in the figure 3.

There are three possible data processing and communication architectures:

- ❑ Remote Processing: the UAV captures the images and sends them to a base station which performs the processing and transmits guidance to the harvesters.

Figure 3 – Representation of the more complex operation architecture: UAV transmitting the orientation of the planting rows in real time.

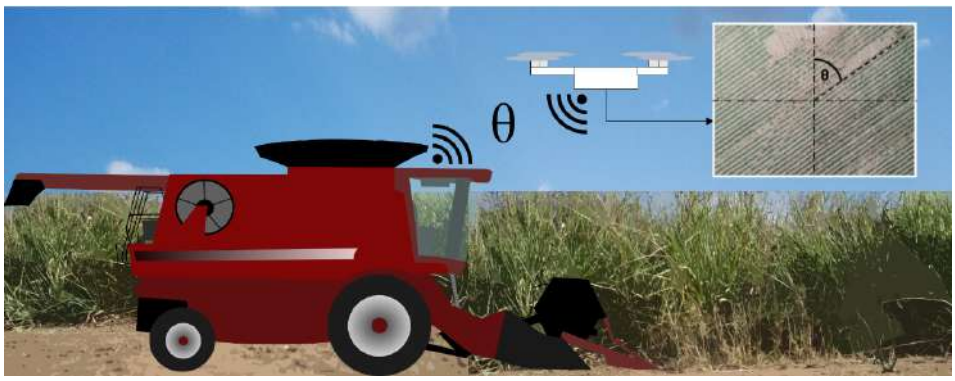

Source: Author.

- ❏ On-board processing: the UAV captures and processes the images, transmitting guidance to the harvesters.

- ❏ Mixed Processing: The UAV captures and preprocesses the images, sending pre-processed images or feature vectors to the base station, finishing the processing and sending guidance to the harvesters.

In this text, we will work with the worst case, which is on-board processing. This means that our goal is to developed an heuristics that can be used as a real-time method to transmit the guidance of the crop lines to the combine. Thus, the processing time to find the orientation is decisive for the success of the task. The processing time constraint requirements for each image are designed based on a combination of cut speed, image overlap percentage, flight height and camera's field of view. The other two cases would be more readily implementable from our study. But before we delve into the specific objectives, we have to detail these two main challenges involved in growing sugarcane: Spacing and Density.

At Harvest operations an important element to consider is the spacing of the crop rows as it allows the optimization of activities such as the intensive use of machines and harvesting. Planting spacing should vary according to the fertility of the land and the characteristics of the recommended variety. In the case of sugarcane, the spacing between furrows can vary from one meter to 1.8 meters. If the harvest is mechanized, the spacing must be at least 1.5 meters to avoid trampling and compaction of the cane lines by the machine wheels. For sugarcane, the so-called pineapple spacing is common, where two rows of sugarcane are planted 0.45 centimeters apart, with a spacing of 1.50 meters between the rows. The total spacing is also 1.80 meters, as shown in figure 4. It is necessary to distribute at least 12 gems per meter of furrow. For planting in times of drought, it is necessary to give preference to a density of 15-18 buds per meter. These

information will be important to define the requirements and acceptance criteria of our proposal later on.

Figure 4 – Crop rows/carrier/harvester distances

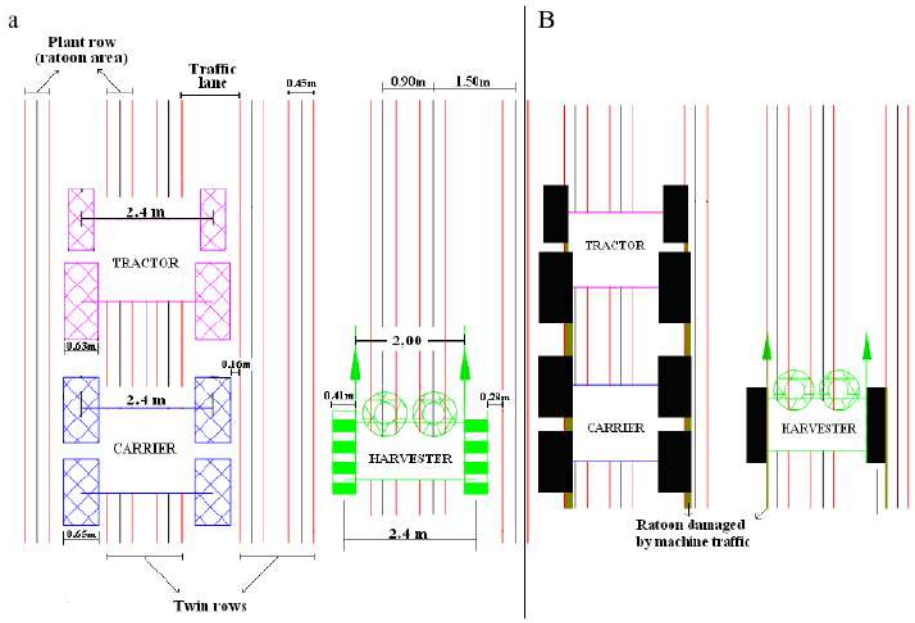

Source: Extracted from Spekken, Salvi e Molin (2014).

As sugarcane can reach a height of up to 2.5 meters and its crowns can blend in with the neighboring planting row, the orthogonal aerial image is adequate to obtain a larger area of the region of interest, as well as to capture more details about line segment patterns, contrasts between soil and plant, as shown in figure 5. As frontal images find application where the crop culture is planted with wide spacing and/or low height, the use of frontal images at low heights such as less than 2 meters is not applicable in sugarcane harvest.

1.3 Objectives and Contributions

The main goal of this work is through image processing and pattern detection techniques to extract from aerial footage of sugar cane plantation its crop orientation angle which is then compared with ground truth measurements.

To implement the proposal, an image database was captured with a commercial UAV and by analysis of human experts generated its ground truth. The proposal was implemented and characterized on a portable computer to qualitatively and quantitatively evaluate the impact of heuristic parameter variations on accuracy and time performance.

This is the summary of the main objectives and other contributions of this work:

Figure 5 – Dense area of sugarcane with the top of the plant blending in with neighboring rows.

Source: Author.

- ❏ A heuristic for detecting and determining the orientation angle of sugarcane crop rows from orthogonal aerial images. based on vertical projections of accumulations of green pixels filtered by Savitzky-Golay techniques;
- ❏ Evaluate the impact of image resolution and algorithms parameters such as scan angle resolution;
- ❏ Compare the developed heuristic with related work based on Radon Transform;
- ❏ A software application for recognition and localization of the crop lines on the images generating a labeled image database used in our tests;
- ❏ A methodology for expert analysis fusion based on the sum of independent and identically distributed random variables.

1.4 Hypothesis

- ❏ The heuristic is capable of extract the crop orientation from images, i.e, the angle where the highest sum value of the Savitzky-Golay filter output occurs reveals the orientation of the cut lines;
- ❏ The performance of the heuristic reaches the necessary time to guide the harvester in a suitable line to pass between the rows of the crop;
- ❏ The heuristic created based on Radon Transform for comparison purpose is capable of reproducing results similar to those found in the literature.

1.5 Thesis Organization

- ❏ In chapter 2 we describe some of relevant state of the art works;
- ❏ In Chapter 3 we present the theory references used in this work such as of computer vision, image processing as well as some statistics important to the understanding of this work;
- ❏ Chapter 4 states the methodology of this project, including the image acquisition process and the datasets used and a description of our approach algorithms;
- ❏ Chapter 5 describes the experimental results obtained for the dataset. Discussions and comparisons between the results obtained by our approach and literature as well as the results obtained by the ground truth measurements;
- ❏ Finally, in Chapter 6 we present the conclusions of this research work, its results, contributions and future work.

Chapter 2

Related Work

As already mentioned before, the popularization of UAV allowed authors to solve several existing problems in agriculture. One of these problems is precisely to identify the existing crop lines in a region and, consequently, their geolocation, layout, as well as the distribution of faults and unevenness in the field. In order to figure out some tendencies and correlation terms used in the recently articles present on Scopus Base in December 2022, a bibliometric analysis was carried out. The analysis consisted of searches with the keywords: *"Remote Sensing"*, *"Detection"*, and *"Crop row"*.

In the search for heuristic techniques, we found terms such as vanishing point, Hough transformation, deep learning, coping, neural network. Beside not present on the image 6, we also find other techniques like, Principal Component Analyses (PCA), Radon Transform. However, most of these approaches either require processing of a crop line at a time, or focusing on plant counting, or even focus on different crop cultures.

2.1 Hough Transform based heuristics

Literature presents some similar approaches to address this problem by identifying the crop lines, many of them are commonly based on the Hough Transform (HT) (HOUGH, U.S. Patent 3 069 654, Dec. 1962), In (BASSO, 2018), the author present a method for crop row detection based on the Hough transform and prior knowledge about the number of crop rows and the row structure. Usage of prior knowledge makes the method tolerant of missing plants and the presence of weeds. In addition, the proposed prior and posterior processing algorithms were fundamental to achieve enhanced performance in the Hough Transform that composes the crop row detection algorithm. However, the Hough transform generates a large number of lines in all directions, it is necessary to filter the

Figure 6 – Bibliometric results

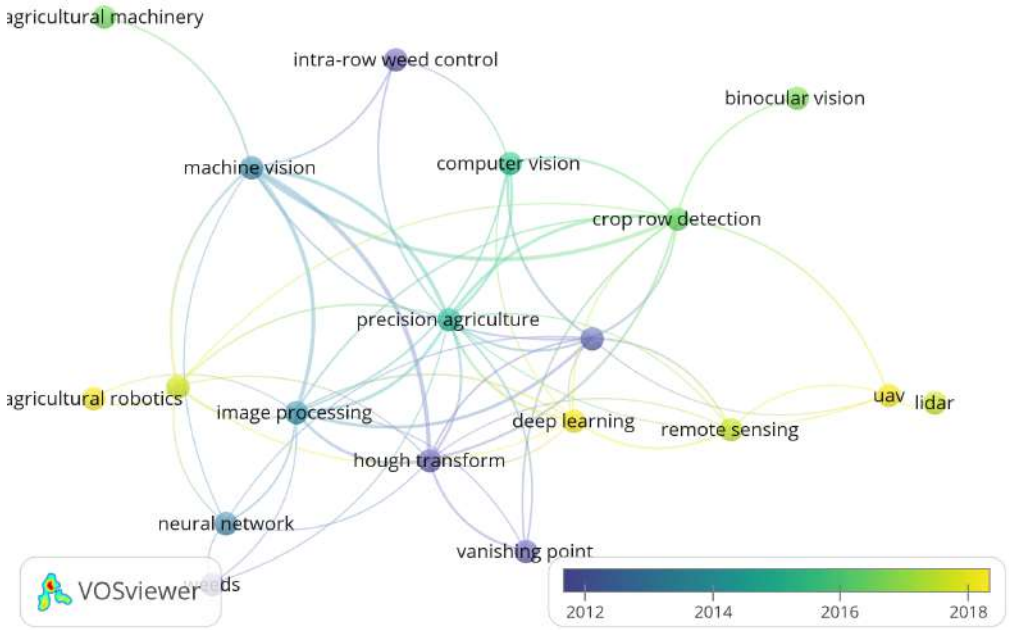

Source: Author.

lines to find the main crop lines. Also, curved lines is not represented correctly by this approach, as shown in figure 7.

2.2 Radon Transform based heuristics

Applying evolutionary techniques with genetic algorithms and the Radon transform, the work of (SILVA, 2020) tries to detect lines of sugarcane plantations, being the work closest to ours. Using this orientation angle it is possible to analyze how the pixels which compose the detected areas are distributed along the image and to detect the center of each crop line in the image. Then, by using the orientation angle of the image and the center of each crop line the authors were able to reconstruct the crop lines with the same constant width as used by the expert.

As shown in figure 8, the proposed scheme for crop line reconstruction using Radon transform: (a) Input image; (b) Matrix obtained with the Radon transform. The red dot represents the location of the maximum point and the orientation angle of the input image; (c) Radon transform obtained for the image orientation angle (red line in (b)). Each peak of the curve corresponds to the center of a line in the input image; (d) Reconstruction of the lines using the orientation angle and the peaks of the Radon transform for that angle.

To evaluate the effectiveness of the method it is necessary to identify separately the error on both segmentation and line detection because the segmentation is a critical step that propagates its mistakes to line identification step. However, the lack of quantitative

Figure 7 – Steps needed by an heuristic based on Hough Transform.

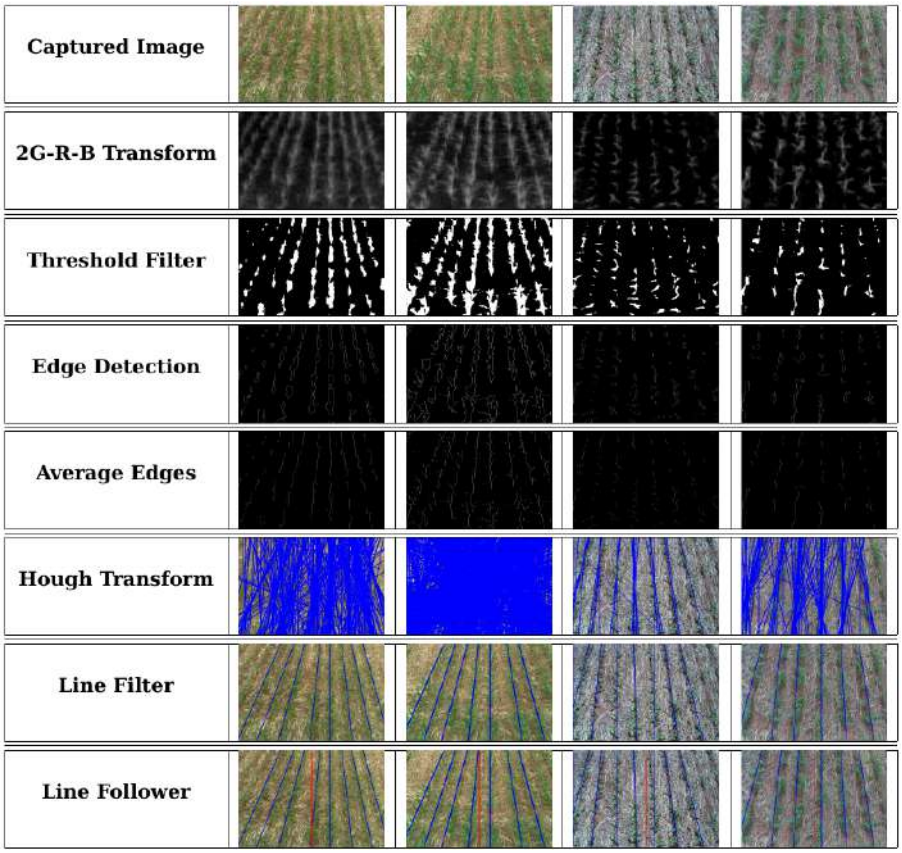

Source: Extracted from Basso (2018).

Figure 8 – Steps needed by an heuristic based on Radon Transform.

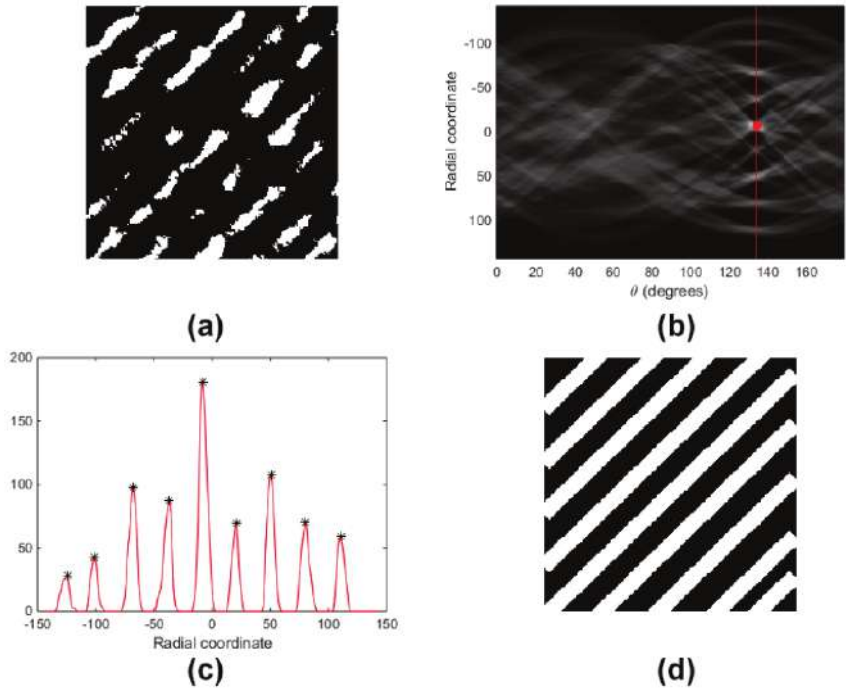

Source: Extracted from SILVA (2020).

analyses regarding the detection error prevented a detailed comparison with our work.

2.3 Others Techniques

There are learning-based approaches, these methods are carried out through supervised and unsupervised learning processes. The training and classification phases are generally off-line and on-line processes, respectively. In the supervised approach, seen in (GUERRERO et al., 2012), the support vector machines (SVM) technique was used in several studies. (BAH; HAFIANE; CANALS, 2018) used a database (knowledge-base) containing samples previously classified. The performance was evaluated through the correct classification percentage and Yule coefficient classified weeds and crop by using 14 features which characterize crops and weeds in images.

The fuzzy clustering technique was used by (YU et al., 2021) to separate the green plants from the soil by applying the famous vegetation indices Excess Green (ExG) defined by (ZHANG; KOVACS, 2012) to segment regions of interest and to differentiate two types of plants (crops and weeds), first discriminating plants and soil and then crop and weeds in the plants (GARCíA-SANTILLáN; PAJARES, 2018).

PCA procedure was used in (HASSANEIN; KHEDR; EL-SHEIMY, 2019) to provide the ability to detect the dominant direction of a data represented in the Principle Component 1 (PC1) along with its perpendicular direction, the Principle Component 2 (PC2). Generally, for any data, PC1 detect the dominant direction of the data, while PC2 indicate how scattered or the variance of this data. Therefore, with the use of PCA for the Hue values in the longitudinal section, PC2 can indicate if the pixels in this section belong to the same type of object or not. This methodology creates different section with small width at different orientations starting from angle 0 to 180 degrees with small step of 1 or less degrees. Through comparing the PC2 values of each section, the crop row orientation theta is detected as the orientation of the section that provided the smallest value of PC2.

In (CARDOSO; FARIAS; SOARES, 2022), a review on the use of UAVs in sugarcane cultivation in Brazil is presented. In general, most of the works focused on identifying gaps in the plantations when the events we try to avoid in our work (crushing of the plants by agricultural machines) have already occurred.

According to the review by (AMARASINGAM et al., 2022), 40% of the sugarcane works analysed use standard RGB cameras (usually sold together with UAVs). About 80 % of the works use quadcopters, as they are cheaper and easier to operate than fixed-wing devices.

(MALDANER et al., 2021) brings an analysis of the use of soil sensors and aerial images in the location and measurement of faults in sugarcane plantations. An interesting result to be highlighted is the identification of a temporal window with the plants at

an age between 31 and 47 days, in which the explored techniques presented their best results. After this time interval, the growth of the plants obscures the view of the ground, impairing the identification of faults. A similar time interval is suggested by (JÚNIOR et al., 2021) (30 to 45 days), with overflights at heights starting at 80 metres, also for the identification of faults in the plantations.

(SOUZA et al., 2017) proposes a heuristic to detect sugarcane flaws in orthoimages using object-based analysis. The authors used a S110-NIR camera as input and, in a early stage of the algorithm, a line detection step was performed. It was achieved by a template matching between a diverse set of line orientation and width. Compared to our work, the authors used a more expensive camera (with near infrared detection) to collect data and the identification is done after all images off the region is collect and the orthomosaic is done.

The use of the KNN (K-Nearest Neighbor) technique as a classifier is proposed in (ROCHA et al., 2020) for the detection of faults in the plantation lines. In its heuristics, the classification step via KNN is followed by segmentation and rotation of the image to determine the angle of more significant variance. A curve fitting is then performed, enabling the identification of curved lines, not only straight ones. However, there is no precise information about identifying the lines, a fact that prevented a direct comparison with our work.

A corn plantation in the early growth stage is monitored in (GARCÍA-SANTILLÁN et al., 2017). Images are taken in perspective, and segmentation is done using the Excess Green technique, similar to the one we used in our work. However, because they are perspective images, their authors use the Hough Transform to detect lines with the aid of the image's vanishing point. Although the pre-processing step is similar to ours, there is no quantitative analysis about the detection of lines, also making impossible a direct comparison with our heuristics. In a later work, the authors complement their paper by adding edges to crop lines and classifiers for (GARCíA-SANTILLáN; PAJARES, 2018) weed identification.

Maise crops in early growth stages suffer greatly from weed incidence. Using perspective imaging, (ZHANG et al., 2018) splits the image into rectangular processing blocks, performs a perspective correction with vertical projection, and finishes with thresholds determining the potential detection of plants in the rows. The division into rectangular blocks allows the identification of interpolation points connected by straight lines. Unfortunately, this work also does not provide detailed quantitative information to compare our results more directly.

This was one of the few papers found with quantitative analysis on the accuracy of line detection. Following the same idea as (ZHANG et al., 2018), the work by (YU et al., 2021) uses block clustering, but this time with a focus on rice crops. The developed technique resulted in errors close to 0.01 degrees applied on perspective images. In this

work, images of the plantation in the early stages of growth were also used.

Deep learning techniques are used in (BAH; HAFIANE; CANALS, 2018) to detect crop rows in aerial images. Applying CNNs (Convolutional Neural Networks), the training of the classifiers is done in an unsupervised way, resulting in an accuracy of 1.5% and 6% in spinach and beans, respectively. We performed some tests with the skeletonisation techniques for image segmentation, similar to this work, but our images' results were not satisfactory.

2.4 Final Considerations

In general, most work in the current literature still focuses on low height crops and/or widely spaced crop rows with clear distinction between crop rows and soil. In these cases, the use of the Hough Transform (HT) technique is widely used. One of the disadvantages of using HT is that the shape of the detected object must be previously known and described, which limits its application. In addition, HT applied to an unstructured environment such as vegetation generates a large number of lines with different angles, making it essential to use optimized filters to obtain only possible candidate lines for the correct orientation.

Another point to highlight is in relation to the type of orientation of the image used in the works observed. Most use images under perspective projection in relation to the crop lines with a camera mounted on land vehicles. In our case, as the cane can reach around 2.5 meters in height at harvest time, it is common for them to be taller than the harvester itself, making the use of the integrated camera unfeasible. Another fact is that it is common for plants from different lines to cross each other, making it difficult to correctly identify the orientation angle of the lines. Choosing low-altitude aerial images (less than 100 meters), which do not require orthorectification to correct perspective errors, is a reasonable choice in this context. In general, the cut lines can be irregularly shaped as they follow the terrain, thus creating curves and irregular shapes, but it is assumed that this can be reduced by keeping the images at low altitudes.

Given this scenario, the work that comes closest to the need for our main objective is the one used by SILVA (2020), in which the Radon transform is the essence of the method, so that this work will be used to compare the results obtained by our heuristic. However, it is worth mentioning that the main objective of SILVA (2020) is to reconstruct the crop lines for failure counting purposes. Furthermore, from the images observed in this same work, the sugarcane is not in the harvesting phase, where line detection becomes less challenging.

Chapter 3

Fundamentals

3.1 Unmanned Aerial Vehicles

Drone is the popular term for unmanned aircraft, because of the noise they make. Broadly, current legislation ((AERONAVES. . . , 2019)) defines any unmanned aircraft as:

> Any device that can sustain itself in the atmosphere, from reactions of the air other than the reactions of the air against the earth's surface, and which is intended to operate without a pilot on board.

Also by law, we can classify unmanned aircraft by take-off weight: class C1 - for aircraft over 150 kg, C2 - for aircraft between 150 kg and 25 kg, and C3 for aircraft weighing less than 25 kg.

Each class has restrictions on registration and access to airspace. The class that will be focused on in this master's dissertation will be the C3 class, respecting the flight ceiling limits (400 feet) and keeping the aircraft in line of sight. Therefore, an authorization in the SARPAS system of the Department of Airspace Control (DECEA) is sufficient.

Within the C3 class, we can separate unmanned aircraft by the lift method. Fixed-wing aircraft, as the name implies, have fixed-wing structures, which are responsible for generating the lift of the entire aircraft in the air, similar to commercial aircraft. These aircraft can have wingspans of a few centimeters to a few meters, and may have one or more propellers that serve as thrusters. On the other hand, rotary-wing aircraft are supported by the thrust force generated by one or more propellers, with the *design* having a lift rotor similar to the helicopter, and, an example, with 4 rotors for lift is the quadrirotor.

3.1.1 Flight range

The flight range of an unmanned aircraft is established in accordance with the legislation in force in the country where the operation will be carried out, even if the equipment is able to perform a greater flight range.

According to Brazilian legislation (ICA 100-40)(AERONAVES..., 2019), the specifications of the UAV used and with the request made for flight, the operations carried out fall within what is called "Operations at very casualties".

Therefore, the flight range established by the same legislation falls under VLOS operation, in which it limits the flight to a distance that allows the visualization and maintenance of the aircraft. VLOS is the acronym for "Visual Line of Sight Operation", which means that in the operation the remote pilot (who is exclusively responsible for handling the pilot controls) maintains direct visual contact with the aircraft, without the aid of lenses or other equipment.

3.2 Computer Vision

3.2.1 Image Acquisition

Image acquisition is the first step of computer vision systems. Its function is to convert the electronic signals from the detection device, such as images from a camera, into numerical representations, which will be used in the following steps (ZAREIFOROUSH et al., 2015) (FILHO; NETO, 1999).

It is commonly called "image acquisition" the process of converting a real 3D scene into a 2D digital scene. The first step of this conversion is the reduction of dimensionality, being the most used devices the sensors with solid state load (CCD or CMOS) (NARENDRA; HAREESH, 2010). The second step of this conversion is digitization. In digitization, the analog signal obtained from the sensor output is subjected to a spatial and amplitude discretization in order to convert the sample to the desired format for the following steps (FILHO; NETO, 1999).

3.2.1.1 Optical camera model

In computer vision studies, cameras are usually modeled from the *pinhole* (STURM, 2014) camera model. The *Pinhole* model (translated as pinhole) is based on the camera obscura principle, where the object's light enters through a small hole (3) (DIAS, 2015) (TONINI et al., 2020). The illustration of the *Pinhole* model can be seen in figure 9 below.

Figure 9 – Pinhole Model

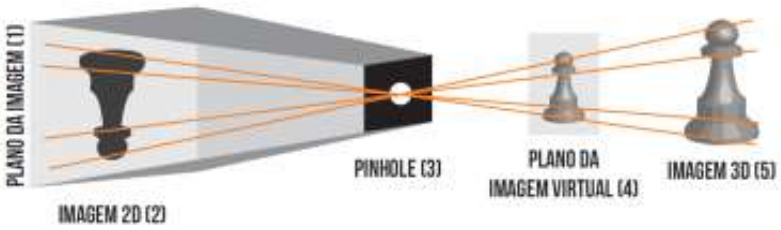

Source: Extracted from Dias (2015)

This model takes into account a central projection, through the optical center of the camera (assuming that the center of the camera is the pinhole) and an image plane (TONINI et al., 2020). In general terms, a 3D object (5) has its 2D projection (2) on an image plane (1) (DIAS, 2015). The main function of the hole is to capture light into the camera and project the image. This projection mechanism is similar to the human eye (DIAS, 2015). In the physical camera, the image is formed mirrored and behind the camera center, however, the image plane is often represented in front of the camera center (TONINI et al., 2020).

The *pinhole* model does not consider that real lenses can produce distortions in the generated images. Distortions are non-uniform stretches of the image, where the center and edges are enlarged by different proportions (DIAS, 2015). Among the existing distortions, the most common is radial distortion, caused by differences in light refraction together with the spherical shape of the (TONINI et al., 2020) lens. This distortion can still be classified into three types, which are: Barrel, Pillow and Mustache.

- ❏ Barrel distortion is usually found in wide-angle lenses, that is, short-range lenses, but with a large field of view. The characteristic that identifies this type of distortion is that the center of the image is larger than the edges (DIAS, 2015);
- ❏ Pincushion distortion is normally found in telephoto lenses, that is, long-range lenses. The characteristic that identifies this type of distortion is that the edges of the image are larger than the center (DIAS, 2015);
- ❏ Mustache distortion is a mixture of barrel and pincushion distortion. The identification characteristic of this type of distortion is that the central part of the image has barrel distortion characteristics and the edges have cushion distortion characteristics (DIAS, 2015).

3.2.1.2 Image segmentation

The aim of image segmentation is to classify an image into specific regions. In order to classify between green plants (crops and weeds) and the background (soil, stones, shadows, etc.), the common method is the application of vegetation indices. Excess Green index

was selected because of its outstanding performance and simplicity (ZHANG; KOVACS, 2012). In a RGB image, the red, green, and blue values, by default, range from 0 to 255. These values have to be normalized in order to calculate the chromatic levels and, thus, obtain the normalized spectral r, g and b components in the range of 0–1. Each pixel can be modified by a mathematical function, so the color of a region of interest can be accentuated, while the unwanted region will be attenuated. Some functions describe combinations between color channels and are therefore called color indices.

The *Excess green* (ExG) is a method that presents good results when applied to separate plants from the bare soil (HAMUDA; GLAVIN; JONES, 2016). This is because ExG provides a clear contrast between plants and soil, and this gives an image of near-binary intensity (MEYER; NETO, 2008). The ExG index has been widely used and has performed well in separating plants and non-plants (MEYER; HINDMAN; LAKSMI, 1998) (HAMUDA; GLAVIN; JONES, 2016) (MEYER; NETO, 2008). The color index balance proposed by (WOEBBECKE et al., 1995) is: $2g - r - b$. Where g, r and b are the chromatic coordinates:

$$\begin{aligned} r &= \frac{R'}{(R' + G' + B')} \\ g &= \frac{G'}{(R' + G' + B')} \\ b &= \frac{B'}{(R' + G' + B')} \end{aligned} \tag{1}$$

Where R', G' and B' are the RGB values normalized between 0 and 1, and are calculated according to the equation below:

$$\begin{aligned} R' &= \frac{R}{R_{\max}} \\ G' &= \frac{G}{G_{\max}} \\ B' &= \frac{B}{B_{\max}} \end{aligned} \tag{2}$$

Where R, G and B are the pixel values of the images based on each channel and R_{max}, G_{max} and B_{max} are each worth 255. The figure 10 shows the effect of Excess Green in a figure where the objective is to highlight the vegetation from the rest of the other elements.

3.2.1.3 Binarization

One of the most segmentation techniques is the binarization, which is defined as the process of converting a RGB or gray-scale image that originally assumed varied color intensity values. After this conversion, the binarized image will assign only two values

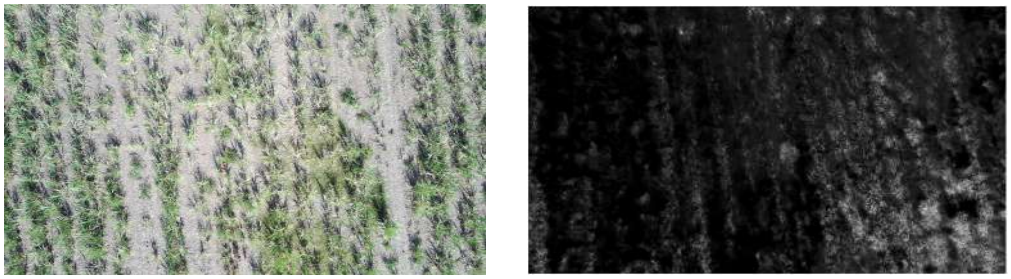

(a) (b)

Figure 10 – Image segmentation process: (a) Original sugarcane image and (b) Vegetable index Excess Green extracted from the original image.

that are typically black and white. One of the most common approaches to calculate a threshold is through the use of Otsu method. This algorithm principally assumes that the image has two classes of pixels following a bi-modal histogram (background and foreground). Besides, the ideal threshold is reached by separating the two classes so that the combined intra-class variation is minimized (OTSU, 1979). There is also image segmentation that's grounded on Otsu's system but iteratively quests for sub regions of the image for segmentation, rather of treating the full image as a whole region for processing, as shown in (CAI et al., 2014). The figure 11 shows the effect of binarization by Otsu on a grayscale figure.

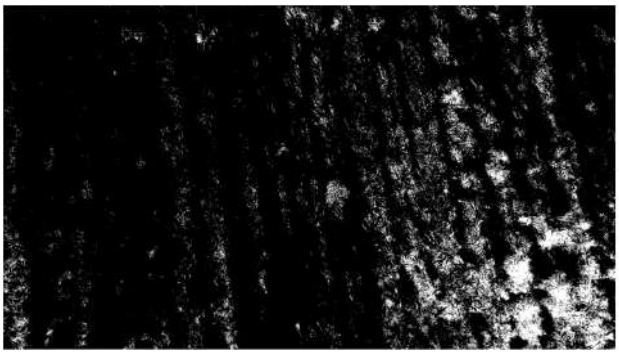

Figure 11 – Image segmentation process: binary image obtained after the first thresholding.

3.3 Image Processing

3.3.1 Down sampling image resolution

The original captured image size is 2716 by 1524 pixels. Usually, with a larger resolution, the image offers more details of the scene. However, to find the angle it was possible to use a downsampled image without a significant loss of information. In addition, in this work application, we used the Gaussian Pyramid function to down sample images as the crop row angle does not depend on image resolution. We used it also to eliminate small

high frequency noises while we still had no loss of relevant information. As the first step in the image processing procedure, Gaussian Pyramid function decreases the computational cost, which impacts the image processing time.

3.3.2 Morphological operations

After obtaining the initial binary image, an extra morphological dilation process is applied to expand the segmented plants. The dilation process can fill the gaps in the plants and the plants appear to comprise a greater number of green pixels (GARCÍA-SANTILLÁN et al., 2017). First, we perform a morphological closing. The closing operation dilates an image and then erodes the dilated image, using the same structuring element for both operations. Morphological closing is useful for filling small holes from an image while preserving the shape and size of the objects in the image. After this, we perform morphological opening. The opening operation erodes an image and then dilates the eroded image, using the same structuring element for both operations. Morphological opening is useful for removing small objects from an image while preserving the shape and size of larger objects in the image. In Fig. 12 we can see the action of the morphological operations applied to the binarized image. The kernel shape and size variation indicate that the image processing techniques are determinant in the crop row orientation measurement exactness. The rectangular kernels have the best results considering the highest fps rate. The size of kernel was locked in 4x4 pixel for close morphological operation and 1x1 pixel for open operation.

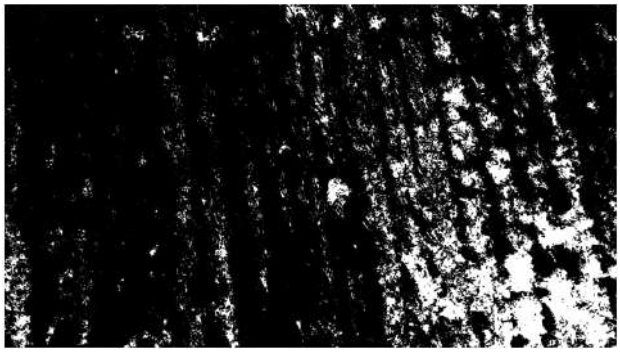

Figure 12 – Image segmentation process: Binary image obtained after the morphological operation.

3.4 Statistical Descriptors

3.4.1 Skewness

It is the measure of how much your frequency curve deviates from the symmetrical position or the measure of the lack of symmetry in a given frequency distribution (CUNHA,

2017). A symmetric distribution is when it presents the same values for the mode, mean and median (CUNHA, 2017) (OLIVEIRA., 2021).

Skewness can be calculated by Pearson's coefficient:

$$A_{\mathrm{S}} = \frac{\bar{x} - M_{\mathrm{O}}}{S} \tag{3}$$

Where x is the mean, M_{O} is the mode, and s is the standard deviation.

The final value of the Pearson coefficient (A_{s}) indicates the presence of symmetry or not, and where the asymmetry is found

- $\mathrm{A_S} = 0$ - Symmetric Distribution;
- $\mathrm{A_S} > 0$ - Positive Skewed Distribution (right);
- $\mathrm{A_S} < 0$ - Negative Skewed Distribution (left).

In figure 13 a positive skewed distribution can be observed in A, in B a symmetric distribution and in C a negative skewed distribution

Figure 13 – Shapes for *Skewness*

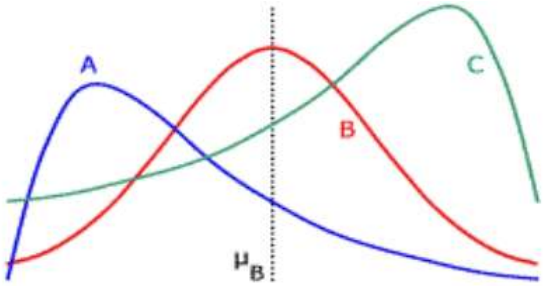

Fonte: Extracted from (KITAHARA, 2021).

3.4.2 Kurtosis

Kurtosis is a measure of the concentration (or dispersion) of data values relative to measures of central tendency of a normal distribution (CUNHA, 2017) (OLIVEIRA., 2021).

Kurtosis can be calculated by the Kurtosis Coefficient:

$$K = \frac{Q_3 - Q_1}{2(P_{90} - P_{10})} \tag{4}$$

Where Q_1 is the first quartile, Q_3 is the third quartile, P_{90} is the 90th percentile, and P_{10} is the 10th percentile.

The final value of the kurtosis coefficient (K) indicates the type of data distribution.

- $\mathrm{K} = 0.263$ - Mesokurtic distribution;

- ❏ K > 0.263 - Platokurtic Distribution;
- ❏ K < 0.263 - Leptokutic Distribution.

In figure 14 a Platokurtic distribution can be observed in A, in B a Mesokurtic distribution and in C a Leptokurtic distribution.

Figure 14 – Shapes for *Kurtosis*

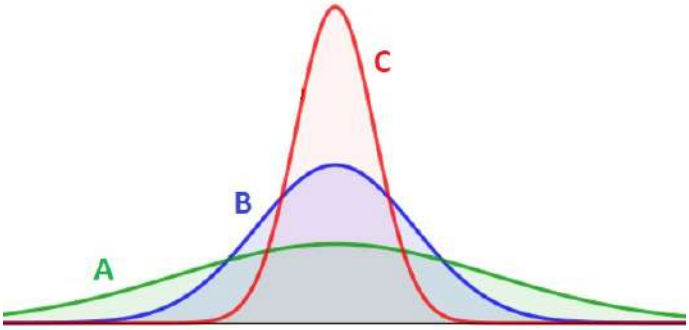

Fonte: Extracted from (KITAHARA, 2021).

3.4.3 Kolmogorov-Smirnov Test

The Kolmogorov-Smirnov (K-S) test is used to decide if a sample comes from a population with a specific distribution, as show in (WANG; WANG, 2010). The Kolmogorov-Smirnov (K-S) test is based on the empirical distribution function (ECDF).

It can be used to approve the null hypothesis that two data populations are drawn from the same distribution to a certain required level of significance. On the other hand, failing to approve the null hypothesis shows that they are from different distributions.

In the one sample K-S test, we are given a sequence of i.i.d. real-valued data samples $z_1, z_2, ..., z_N$ with the underlying cumulative distribution function (cdf) $F_1(z)$, and a hypothesized distribution with the cdf $F_0(z)$. The null hypothesis to be tested is

$$H_0 : \quad F_1 = F_0 \tag{5}$$

The K-S test first forms the empirical cdf from the data samples

$$\widehat{F_1}(z) \doteq \frac{1}{N} \sum_{n=1}^{N} \mathbb{I}(z_n \leq z) \tag{6}$$

An attractive feature of this test is that the distribution of the K-S test statistic itself does not depend on the underlying cumulative distribution function being tested. Another advantage is that it is an exact test (the chi-square goodness-of-fit test depends on an adequate sample size for the approximations to be valid).

Figure 15 – Comparison between two cumulative probability of distributions.

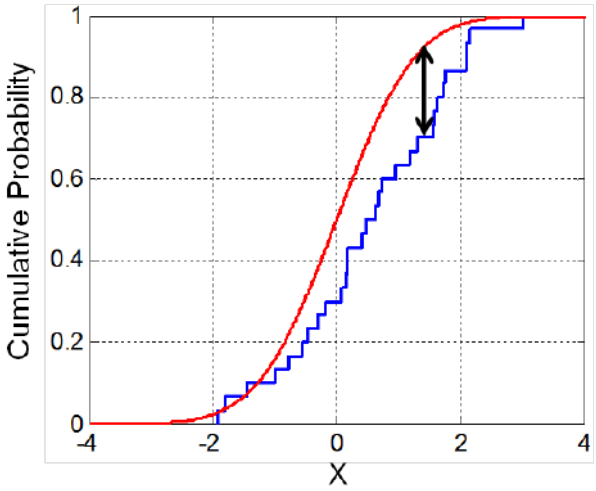

Source: Extracted from Wikipedia contributors (2022).

3.4.4 Algebraic operations between independent random variables.

Consider the problem of estimating the common mean of two normal distributions with independent estimators for variances. The results in (TARABA, 2021) provides sufficient conditions for the combined estimator to be better than the uncombined estimator in terms of making its variance smaller.

$$\mu_{new} = \frac{\sigma_2^2}{\sigma_1^2 + \sigma_2^2}\mu_1 + \frac{\sigma_1^2}{\sigma_1^2 + \sigma_2^2}\mu_2 \tag{7}$$

$$\sigma_{new}^2 = \left(\frac{1}{\sigma_1^2} + \frac{1}{\sigma_2^2}\right)^{-1} \tag{8}$$

Combining the second and third models first and then combining the result with the first model would lead to the same optimal blending parameters. The order of the combination is inconsequential. In figure 16 shown three variables and its combined resultant. The combined distribution has a lower standard deviation compared with smaller of the original distributions.

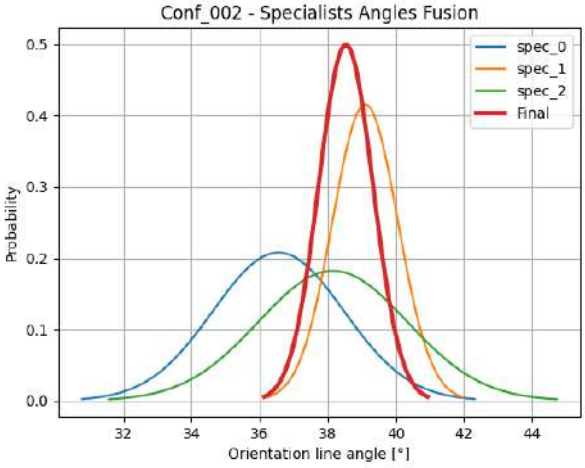

Figure 16 – Fusion measurements

3.4.5 Outliers detector

In statistics, the median absolute deviation (MAD) is a robust measure of the variability of a univariate sample of quantitative data. It can also refer to the population parameter that is estimated by the MAD calculated from a sample. For a univariate data set $X_1, X_2, ..., X_n$, the MAD is defined as the median of the absolute deviations from the data's median $\tilde{X} = median(X)$:

$$MAD = median(\mid X_i - \tilde{X} \mid) \tag{9}$$

that is, starting with the residuals (deviations) from the data's median, the MAD is the median of their absolute values.

For normally distributed data, the scaled MAD is approximately equal to the standard deviation.

$$\lim_{n\to\infty} E(m(x)) = \sigma\Phi^{-1}(0.75) \tag{10}$$

where $\Phi^{-1}(0.75) = 0.6745$ is the 0.75^{th} quantile of the standard normal distribution and is used for consistency. That is, so that $m(x)/0.6745$ is a consistent estimator of the standard deviation σ.

If you can't assume normality, you can use the 0.75^{th} quantile of any other distribution that is symmetric about some value (not necessarly the mean) standardised to have mean 0 and standard deviation 1. Typically a t-distribution is used if fat-tail are assumed. (IGLEWICZ; HOAGLIN, 1993) suggest using ± 3.5 as cut-off value but this a matter of choice (± 3 is also often used).

3.5 Savitzky-Golay Filter

As the sinogram generated by the radon transform only shows the accumulation of pixels projected in a given direction, our method will go further to obtain the variation of pixel accumulation during rotation. This is because when the cut lines are aligned with the vertical axis we will have the maximum variation in intensity accumulation. For this, we will use a widely known filter, the article by Savitzky and Golay is one of the most cited articles in the journal Analytical Chemistry (LARIVE; SWEEDLER, 2013).

The following equation defines the general filter equation according to Savitzky and Golay. The particular behavior of the filter can be influenced by choosing appropriate filter coefficients. Thus one can generate both the moving average filter, the polynomial fit, and the smoothed derivatives simply by adjusting the coefficients of this equation.

$$Y_j = \sum_{i=\frac{1-m}{2}}^{\frac{m-1}{2}} C_i \, y_{j+i}, \qquad \frac{m-1}{2} \leq j \leq n - \frac{m-1}{2} \tag{11}$$

In (SADEGHI; BEHNIA; AMIRI, 2020), Savitzky-Golay is a digital filter that can be applied to a set of digital data points in order to smooth (or derive from the smoothed signal) the central point of each data subset, i.e, increasing the accuracy of the data without distorting the signal trend.

The application that first motivated Savitzky was to localization of maxima and minima in experimental data curves (SAVITZKY, 1989). The first derivative of a function is zero at a maximum or minimum, also linear interpolation of the first derivative values at positions either side of the zero-crossing gives the position of the peak maximum.

3.6 Radon Transform

The Radon Transform is an important mathematical tool in the field of image analysis. It was proposed by Johann Radon in 1917, and represents projection if a function obtained in a specific orientation, being considered the basis of classical tomography (SILVA, 2020).

From (RADON, 1986) the Radon Transform of a function $f(\mathbf{x})$ presuppose that $f(\mathbf{x}) = f(x, y)$ is a function that satisfies the three regularity conditions:

1. $f(\mathbf{x})$ is continuous;
2. the double integral $\iint \frac{|f(\mathbf{x})|}{\sqrt{x^2+y^2}}\, dx\, dy$ extending over the whole plane, converges;
3. for any arbitrary point (x, y) on the plane it holds that

$$\lim_{r\to\infty} \int_0^{2\pi} f(x + r\cos\varphi, y + r\sin\varphi)\, d\varphi = 0.$$

The Radon transform, Rf, is a function defined on the space of straight lines $L \subset \mathbb{R}^2$ by the line integral along each such line as:

$$Rf(L) = \int_L f(\mathbf{x})|d\mathbf{x}|.$$

Concretely, the parametrization of any straight line L with respect to arc length z can always be written:

$$(x(z), y(z)) = \Big((z\sin\alpha + s\cos\alpha), (-z\cos\alpha + s\sin\alpha)\Big)$$

where s is the distance of L from the origin and α is the angle the normal vector to L makes with the X. It follows that the quantities (α, s) can be considered as coordinates on the space of all lines in $\mathbb{R}^2$, and the Radon transform can be expressed in these coordinates by:

$$\begin{aligned} Rf(\alpha, s) &= \int_{-\infty}^{\infty} f(x(z), y(z))\, dz \\ &= \int_{-\infty}^{\infty} f\Big((z\sin\alpha + s\cos\alpha), (-z\cos\alpha + s\sin\alpha)\Big)\, dz. \end{aligned}$$

The Radon transform data is frequently called a sinogram because the Radon transform of an out-of-center point source is a sinuosity. therefore, the Radon transform of a number of small objects appears graphically as a number of blurred sine swells with different amplitudes and phases.

Chapter 4

Methodology

4.1 Unmanned Aerial Vehicle

The type of unmanned aerial vehicle chosen to be used in the development of this project was a Fimi X8 SE quad-rotor.

Figure 17 – Drone modelo FIMI X8 SE

Source: Author.

It records 4k HDR videos, has 3-axis *gimbal* engine, portable *design*, intelligent tracking and flight mode, 8KM signal range, 35 minutes of autonomy flight, visual positioning system Accurate, rainproof, built-in camera, remote control, real-time GPS.

4.1.1 Technical specifications

The technical information below is according to the official website of the Fimi brand (FIMI. . . , 2021).

- ❏ Dimensions: 204 X 106 X 72.6mm;

- ❏ Maximum speed: 18m/s;
- ❏ Flight altitude limit: 500m;
- ❏ Weight: 765g;
- ❏ Wind resistance: $\leq 50kph$;
- ❏ Accuracy:
  - $\pm 0.1m$ (without the ultrasonic detection range);
  - $\pm 0.5m$ (with GPS positioning enabled).

4.1.1.1 Stability of *Gimbal*

- ❏ Controlled rotation range: $0\ ^\circ \sim -90\ ^\circ$ Tilt angle;
- ❏ Angle control precision: $\pm 0.004\ ^\circ$;
- ❏ Stabilization: 3-axis gimbal

4.1.1.2 Integrated camera

As mentioned above the UAV has an integrated camera. Camera specifications are presented in the subsections below:

- ❏ Model: The built-in camera type is RGB;
- ❏ Maximum photo resolution: 4000 * 3000;
- ❏ Video resolution:
  - 3840 x 2160 30/25/24fps;
  - 2560 x 1440 60/50/30/25/24fps;
  - 1080P 100/60/50/30/25/24fps;
  - 720P 200fps.
- ❏ Image format: JPG; JPG+DNG;
- ❏ Video format: MP4;
- ❏ Lens aperture angle:
  - Lens: FOV 80 °;
  - Aperture: f2.0;
  - Focal length: 3.54mm;

– Equivalent focal length: 26mm;

– Sensor: 1/2.6" SONY CMOS;

– Effective pixels: 12M;

– ISO range: 100 - 3200;

– Shutter Speed: $32 \sim 1/8000s$.

The main advantage of using a drone with an integrated camera is the lower cost compared to adapting another camera. However, the disadvantage is that you are limited in the type of cameras, not being able to make use, for example, of a multi/hyper-spectral camera.

4.1.2 Coordinates Systems

With the coordinates of the axes of the points of the lines, it is related to the length and angle of the vertical lines, which can vary from -90° according to the image. This is because, the lower axes and tips of the drone work in NED (North, East and Down) mode. X axis points to north, axis and axis to east and z to tips.

Figure 18 – 3D view of NED coordinates system

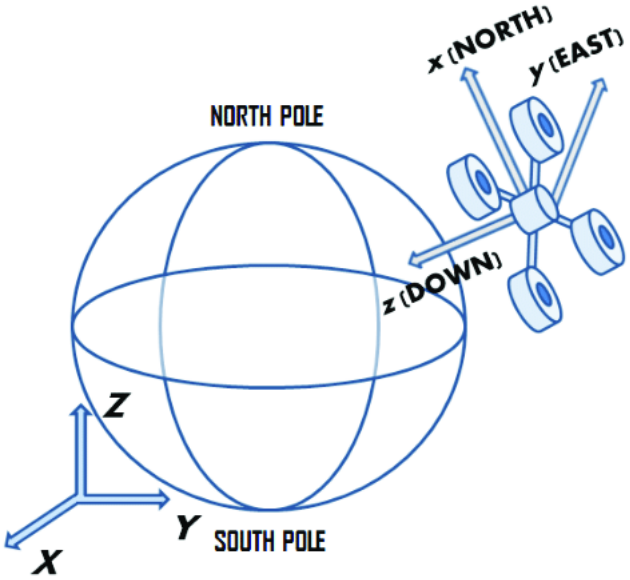

Source: Extracted from Giernacki, Goslinski e Espinoza-Fraire (2021).

Figure 19 – 2D view of NED coordinates system

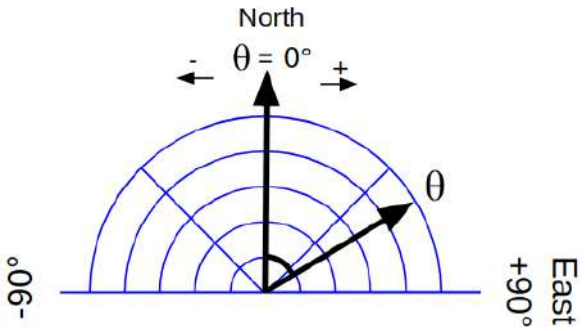

Source: Author.

4.2 Image acquisition - Dataset

The flights were executed during the month of May 2021 at São Carlos and Monte Aprazível cities of State of São Paulo - Brazil, with flight height varying between 20 to 40 meters. From those flights, 40 images were selected. It was observed a minor perspective issue given by terrain declivity. Images with different culture line orientations were captured in order to provide heterogeneous data in the study. Fig. 20 shows two illustrative examples in different sugarcane growing environments under conditions comprising (a) high weed and gaps, and (b) low weed and high height.

The images are free of perspective projection because they are acquired with the camera in an orthogonal position. Its camera is attached to a 3D gimbals, oriented orthogonality to the ground with a resolution of 2700 × 1500 pixels.

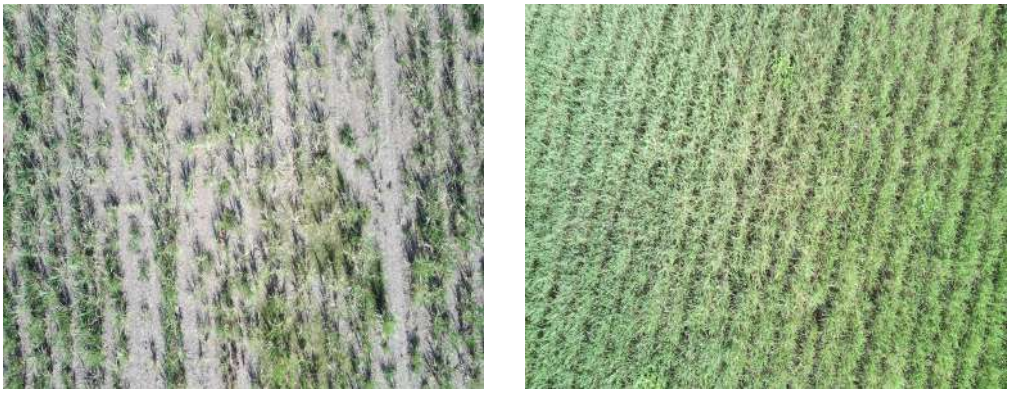

(a) (b)

Figure 20 – Original images with various sugarcane situations: (a) presence of gaps and weeds, (b) sugarcane high height.

The weather conditions during the flight can greatly affect the performance of the drone. Factors such as wind, rain, and fog can make it difficult for the drone to maintain stable flight and accurately capture images. The terrain over which the drone is flying

can impact its performance. Rough or hilly terrain can make it more challenging for the drone to maintain stability and accurately capture images. The flight altitude of the drone can impact its performance. Flying at higher altitudes can increase the risk of the drone encountering adverse weather conditions, while flying at lower altitudes can increase the risk of collision with obstacles such as trees and buildings.

4.3 Programming Language

Founded in 1991 by Dutch developer Guido van Rossum, *python* is a high-level, dynamic programming language. Its versatile features and syntax help programmers to develop code in fewer steps and in fewer lines compared to Java and C++ language.

The *python* language has several application possibilities, both in academic and business environments. Its advantages over other programming languages are:

- ❏ Open source;
- ❏ Libraries: *python* has large standard libraries already implemented that include areas such as *string* operations, internet, web service tools and operating system interfaces. This means that most programming tasks that are heavily used are already programmed, which results in shorter code lengths;
- ❏ Ease of learning and coding;

Its disadvantages include:

- ❏ Low usage in mobile computing;
- ❏ Its execution is carried out through an interpreter, while other languages make use of compilers. This causes it to be slow, depending on the application;

We chose to use this language because there are several ready-to-use modules, such as the Savitzky-Golay filter, Radon transform, which allowed us to focus on choosing and testing the best parameters and adjusting them to our application. Below are the references of the main modules used in this work:

- ❏ OpenCV (Open Source Computer Vision Library) is a library of programming functions mainly aimed at real-time computer vision. This is the main module that contains the most common tools in terms of image processing. We used to convert color, resize image, import and save, rotate, Otsu limit and morphological changes.
- ❏ There is a function from SciPy library that enables the use of Savitzky-Golay filter. It is possible to select the length of the filter window, the order of the polynomial

used to fit the samples, derivative order to calculate among other parameters to generate the filtered data. SciPy also contains modules for optimization, linear algebra, integration, interpolation, special functions, FFT, signal and image processing, ODE solvers and other tasks common in science and engineering.

- From Scikit-image library we used the radon function available to forward transform our images. The input parameter is the number of projection angles we wish to use to generate the sinogram.

4.4 Ground Truth Generation

In order to evaluate the performance of the developed methodology, it is necessary to compare the final result with the result of a human expert. The methodology used to obtain the absolute truth is represented in figure 21 and will be explained below.

To mitigate the biases of a single expert, 5 experts were asked to establish the ground truth of the dataset, that is, the average orientation of the crop row in each image of the dataset. In most applications that use the image, the ground truth is unknown before the scene image, as the scene may contain distinct elements that change the orientation of the lines, such as weeds, terrain contours, lack of line parallelism, shrouded lines by vegetation, imperfections in the cultivation line that generate imprecision and uncertainty in determining the ground truth. In this type of applications, the reality is unknown and different experts can propose line angles for the scene.

To help with the task of establishing ground truth, a software application was specifically developed to allow lines to be drawn over the available images in the dataset. One can draw as many lines as possible. At the end of marking, the coordinates of the two points that represent the limits of the lines are saved as well as the number of marked lines.

Figure 22 – Software labeling

Source: Author.

With the coordinates of the points, the length and angle of the crop row in relation to the north vertical axis are calculated, as shown in the image. Lines with a length of less

Figure 21 – Diagram of the proposed approach to the problem.

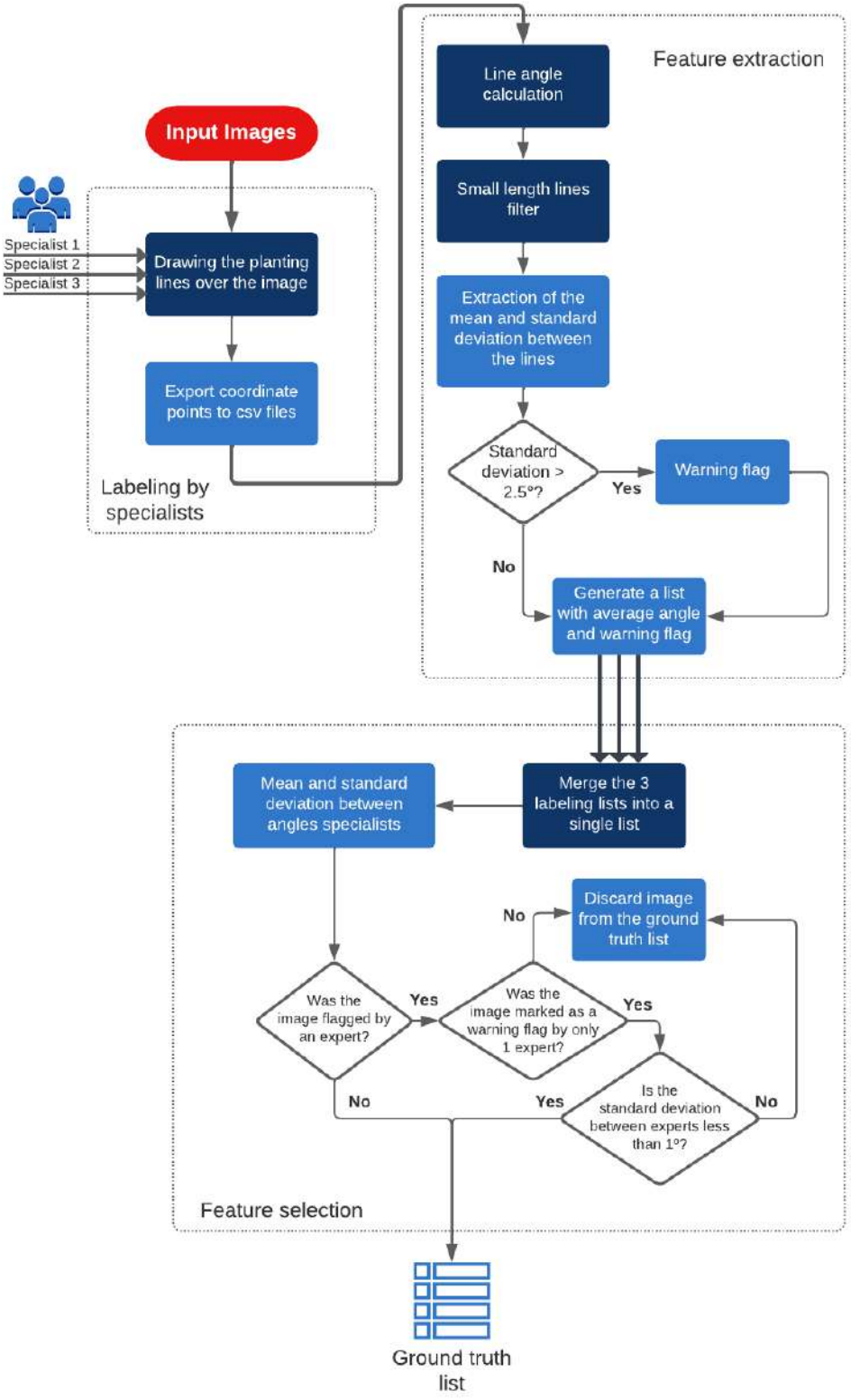

Source: Author.

than 50 pixels are discarded, as they bring about imprecision in the ground truth, since a good marking of the cultivation line must cover a good part of the image. The mean of the angles and the standard deviation of the set of marked lines that pass through the filter are taken. If the standard deviation of the angle between the marked lines for a given image is greater than 2.5°, it will be marked as a warning flag. The image is not discarded immediately, as it will be compared with the results of other experts later. In order to compare the marks of each expert, the average angle and warning flag information of each image are gathered in a single comma-separated values (csv) file extension.

Since each expert pointed out a different result for the crop row angles, it is difficult to determine which result to choose, because there is no objective standard of choice. For that, we need to merge the information from each expert into a single result. We will take the average of these results. As each result has its own uncertainty (since several lines have been drawn, a mean value and a standard deviation are generated) and are independent of each other, we can form a new result, that is, a new distribution by combining the 5 values originated by experts. But before that we need to carry out a preliminary test to know the equality of variances, that is, whether the experts' scores follow a normal or a Gaussian distribution, according to the Kolmogorov-Smirnov (K-S) normality test, presented in the background section.

The results of the Kolmogorov-Smirnov test confirmed the normal distribution of the variance of the crop lines pointed out by each of the experts, so we can do some classic statistical procedures, among them, the average between the 5 distributions of the experts. The combination of 5 normal distributions follows the equations of shown in Guerrero et al. (2012)taraba and the Fundamentals chapter. This creates a new mean angle and standard deviation for each image, and this represents the ground truth of the mean orientation of the crop lines.

The last step is to apply a filter that eliminates images that are not suitable for the ground truth. An image is not suitable for the ground truth when the crop lines marked by experts have a standard deviation greater than 2.5° or when the combined standard deviation across all experts is greater than 1.5°. The filter logic is represented in figure 21. If the image is in the warning list by only a single expert, the combined standard deviation is analyzed, if it is less than 1.5° the image will remain as ground truth, otherwise the image will be discarded. If the image is on the warning list of two or more experts, the image is automatically removed from the ground truth.

4.5 Proposed Heuristics

In this section, we will discussed in detail the proposed solution based vertical projections of accumulations of green pixels filtered by Savitzky-Golay. The figure 23 illustrates the overall strategy adopted in this work.

Figure 23 – Diagram of the proposed approach to the problem.

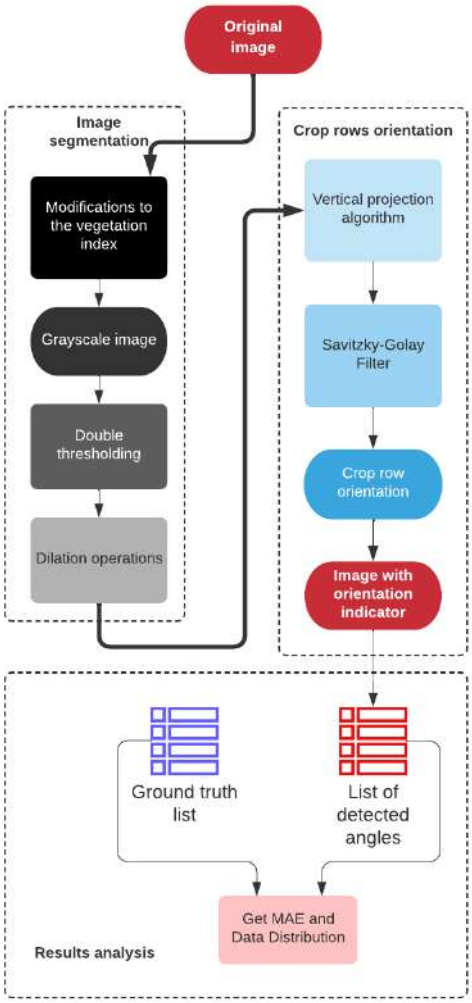

Source: Author.

Image segmentation

As can be observed, Figure 23 divides our algorithm in two parts, Image Segmentation and Crop rows orientation. The first module of our heuristic consists of a transformation using the Excess Green Vegetation Index (ExG), as presented in (GARCÍA-SANTILLÁN et al., 2017). The output of this stage is a grayscale image in which plants (generally green) are highlighted in contrast with soil, as shown, for instance, in Figure 10(b).

Given the grayscale image after the ExG application, a global threshold method was applied, to achieve a binary image. The chosen method was the global Otsu threshold, leading to a black and white image, as seen in Figure 11.

As seen in Figure 12, there are a few pixels scatterd alone in the image, and in places where should have been only white there are few black dots. Thus, for the binarized image, a set of morphological operations can refine it.

This step was divided into two parts, a closing operation (dilatation followed by erosion) with a rectangular structural element of 4 by 4 pixels, the a open operation (erosion

followed by dilatation) of 1 by 1 rectangular kernel. The final result is presented on Figure 12.

Crop Rows Orientation

The second part of our heuristic starts with the projection algorithm, which was inspired by Rocha et al. (2020). We perform a rotation of the image from $-90°$ to $90°$, with the angular resolution being left as tuning parameter. For each rotation step, the sum of white pixels is done per column, thus creating a projection vector.

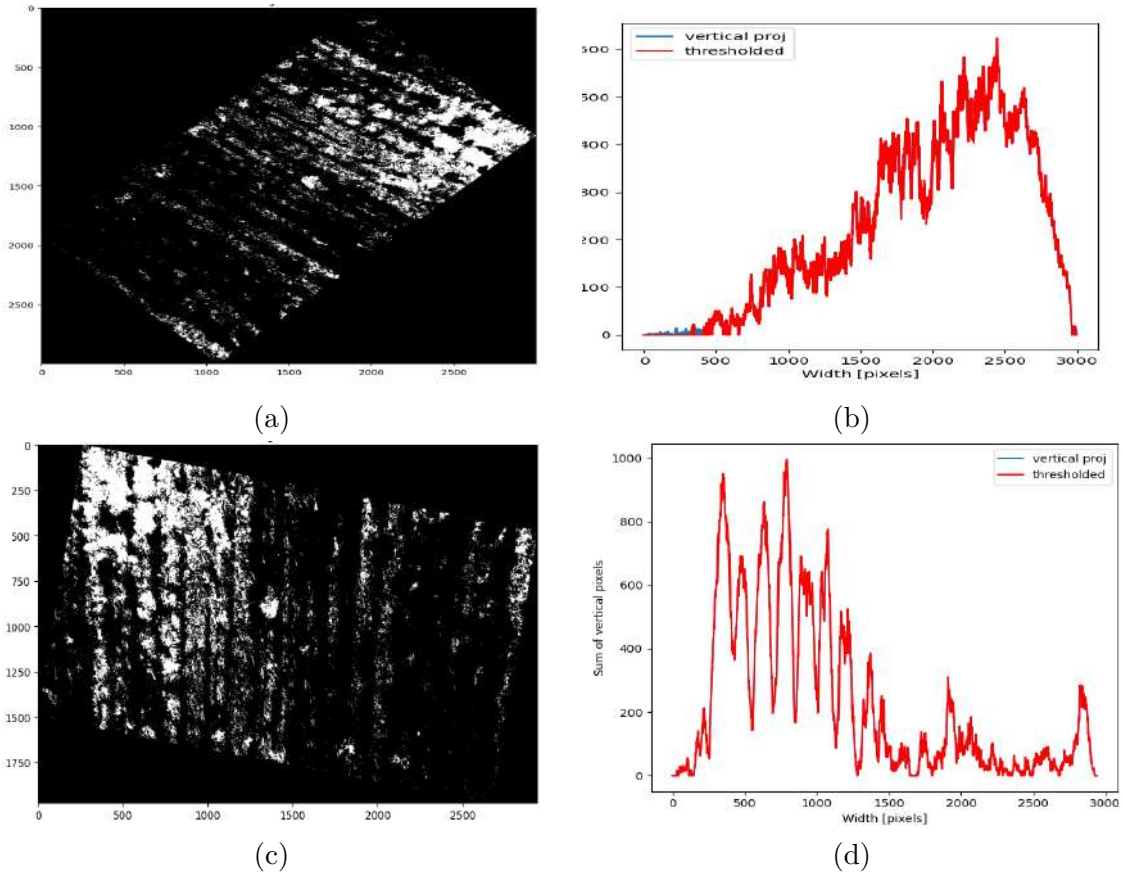

Figure 24 – Vertical projection algorithm steps: (a) and (c) image rotated in specific angle; (b) and (d) respective vertical projection curves

Figure 24 illustrates what happens to the projection vector as the angle of rotation shifts. Figure 24 (a) and (c) show the result of image rotation and Figure 24 (b) and (d) its respective projection vectors. When the lines starts to be aligned in the vertical orientation, the signals presents well-defined peaks and valleys, which characterizes the plantation line and inter-row exposed soil.

Based on Figure 24d, when the orientation of the crop line is parallel to the vertical axis, the greatest variation in the vertical projection vector will occur. Now we just need to identify the rate of change, regardless of the magnitude of the accumulated value. For this, we will use the Savitzky-Golay filter (SADEGHI; BEHNIA; AMIRI, 2020). It was

chosen the second order first derivative configuration and the window size was left as a tuning parameter. After that, a simple threshold is applied to the output vector Y_j to detect only high variation and then creating an vector **z** that contains the number of occurrences of non-zeros values of the output vector. The final angle θ_f is obtained from the largest elements of **z**.

The output of the Savitzky-Golay filter reveals the variation of the sum of intensity of the vertically projected pixels as a function of the image rotation angle. The angle where the highest value of the filter output occurs reveals the orientation of the cut lines.

As can be seen in the Fig. 25, a maximum peak at 19° from all values from array **z**. This means that the orientations of the planting lines is aligned with the projection direction, thus it is possible to visually confirm the method's assertiveness.

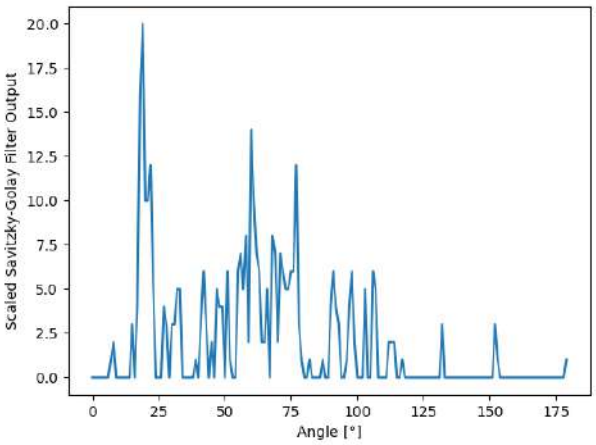

(a)

(b)

Figure 25 – (a)Vector of pixels variances and (b) Sugarcane image with line drawn by algorithm.

4.5.1 Heuristic Replication of Literature for Comparison

In this subsection, we present a heuristic based on Radon Transform for reproducing the technique and results used by SILVA (2020) for the purpose of comparison with the heuristic created in this work and explained previously. The figure 26 illustrates the overall strategy adopted to replicated the Radon-based Heuristic.

Figure 26 – Diagram of the proposed approach for Radon Transform heuristic.

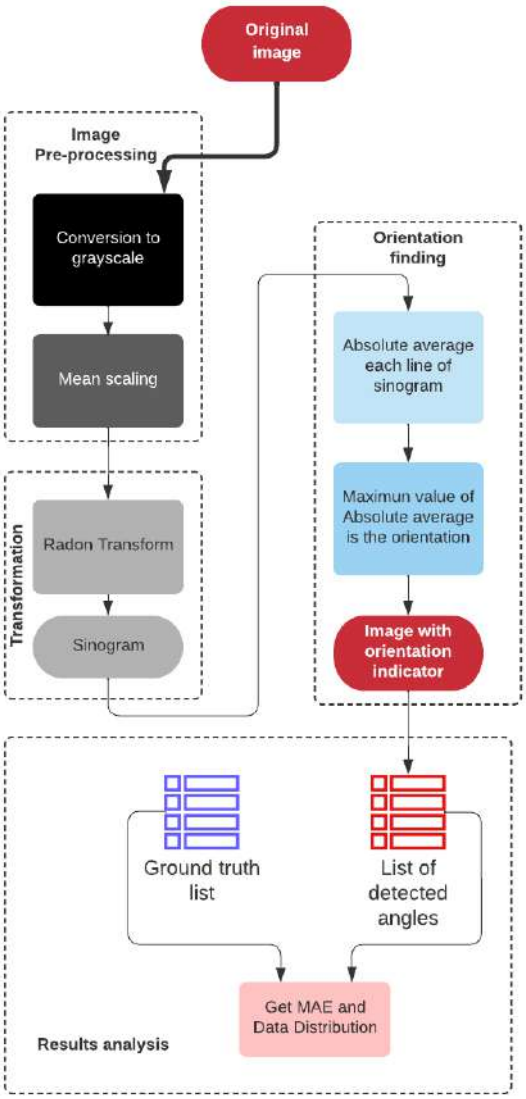

Source: Author.

As can be seen, Figure 26 divides the proposal into three parts, image pre-processing, transformation and orientation discovery. It is important to emphasize that both the first and the last part of this strategy were not taken from SILVA (2020) work, since his objective was the reconstruction of crop lines. We also chose to simplify the pre-processing so that this process has the least influence on the Radon transform which is the essence of the approach here.

The first pre-processing step is to apply a classic grayscale conversion given by the equation below:

$$Grayscale = \frac{R + G + B}{3} \tag{12}$$

Then, scaling the image by subtracting all pixels from the average grayscale value of the image. The results of these steps are shown in the figure 27

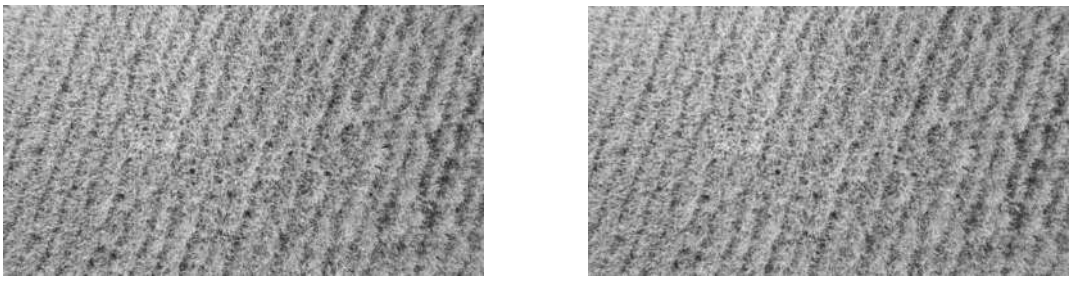

(a) (b)

Figure 27 – (a) Image converted to grayscale and (b) Grayscaled image decreased by the mean.

Source: Author.

In figure 28(a) we can see the image 27(b) applied to the radon transform. Vertical projections through the crop row image result in an accumulated signal. The sinogram is generated by collecting many such projections as the crop row image rotates. Here, intensity is used to highlight the accumulated signal. Note how straight crop row, when aligned with the projection direction, result in stronger signals.

With the sinogram image generated we have to extract the feature of interest which is the angle where occurs the maximum intensities which in turn means the crop row angle orientations of the original image. In order to achieve this we have to apply a simple absolute average at all of the pixels present in each column of the sinogram to turn it into a single intensity value per angle. From equation 13 **n** is the index for each element of sinogram's column.

$$I = \frac{\sum_{i=1}^{n} |y_n|}{n} \tag{13}$$

Applying this intensities formula to each column of sinogram generates a figure shown in 28(b) where all absolute average intensity values are ordered by angle of occurrence.

We can see a very strong intensity peak at 161°. This means that the orientations of the planting lines is aligned with the projection direction. But before we draw a line with the detect orientation angle on the image we have to convert this angle to our NED system coordinates.

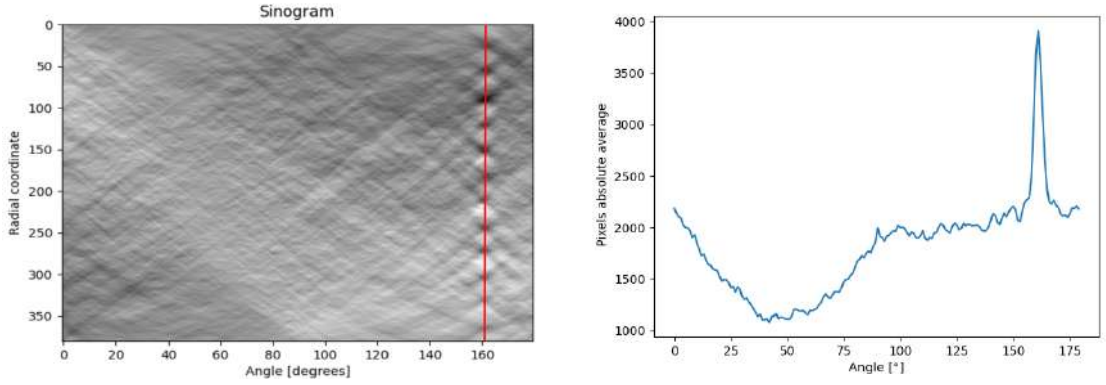

(a) (b)

Figure 28 – (a) Sinogram (b) Sinogram's pixels intensity sum filtered and ordered by rotation angle.

Source: Author.

4.6 Definition of project requirements

The algorithm must meet the time and accuracy requirements to integrate the harvest mission. This subsection explains how parameters affect the final result and a correct choice for them.

4.6.1 Down View

The main design parameter that affects both time and accuracy is the flight height of the UAV, represented by h in the figure 29. The value of h is the flight height of the drone and can be obtained both during the flight, through the control interface, and through the properties of the image obtained.

Figure 29 – Down view

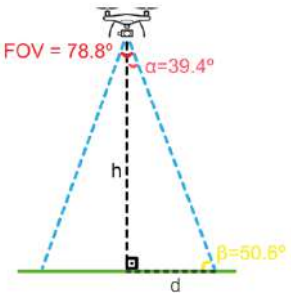

Source: Author.

The greater the height h, the greater the coverage area of the image. So, let's first calculate the coverage area of the image as a function of height. Using the *Pinhole* model, it is possible to use trigonometry to estimate of the size, in meters, of the sides of the figure 30. It is known that the sides on the image have side dimensions x in 2716 *pixels*, and y in 1524 *pixels*.

Figure 30 – Dimensions of the images obtained by the drone

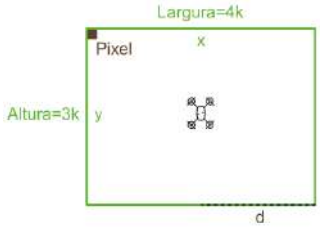

Source: Author.

To find the value of d of figure 29 and 30, it is necessary to assume that the drone is flying parallel to the ground, so that its height h forms a 90 degree angle with the ground. Another consideration is the camera lens aperture angle was given in the technical specifications as being equal to θ, with this information and using basic trigonometry, one can calculate the angle α according to the formula $\alpha = FOV/2$. Our camera has $\theta = 78.8$ degrees, this results in a value of $\alpha = 39.4$ degrees.

The relationship between d, α e h is given by:

$$d = \tan(\alpha).h \tag{14}$$

The length x of figure 30 is twice the distance d. Therefore, x and y respectively maintain the following relationships with the flight height of the UAV:

$$x = 2.\tan(\alpha).h \tag{15}$$

$$y = 0.59(x) \tag{16}$$

Plotting a graph with various values for the height of flight, we see the linear relationship with the lateral dimensions represented by the image.

4.6.2 Minimum flight height

From the graph in the figure, we can establish the first design constraints. From preliminary tests, it was defined that for the algorithm to have good results in terms of accuracy in identifying the orientation of crop lines, the image must contain at least 10 crop lines containing at least 15 plants present in each line. According to the information contained in the introduction, we know that the spacing between cultivation lines can reach 1.8 meters and the density of cane planted in each line can reach 1.2 linear meters between each plant. Thus, the minimum dimensions of the sides of the image are:

$$y = 15 * 1.2 = 18m$$

Figure 31 – Image side dimensions

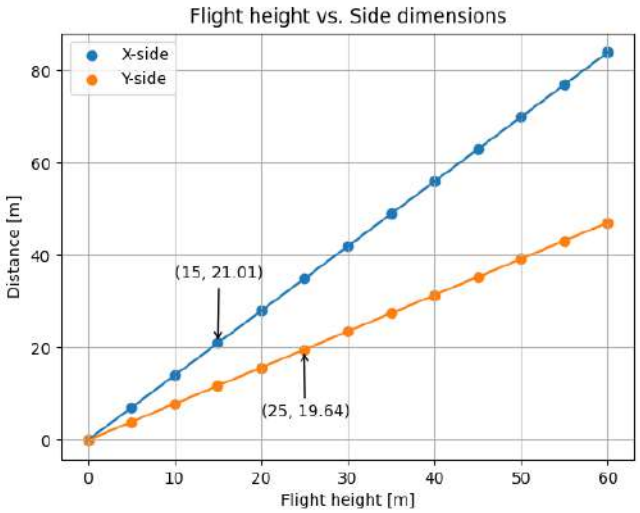

Source: Author.

$$x = 10 * 1.8 = 18m$$

Minimum dimension values are marked on the chart. The flight height that meets both requirements will be above 25 meters.

4.6.3 Maximum flight height

The higher the height of the drone, the lower the number of pixels that define the contrast between the lines of vegetation and the ground, making the algorithm have an extremely difficult work and carrying inaccuracy of the result. To calculate the UAV's maximum flight height, we took into account the physical distance between crop row spacings, viewed from above. Right after planting the seedlings, the distance is 1.8 meters, that is, we have 1.8 meters of soil in aerial view. However, as the plant increases in volume, the view of the ground is obscured, mainly by the leaves of the plantation. In our studies, we observed that a sugarcane field in the harvesting phase has, on average, only 40 cm of soil. So we want these 40 cm of soil to be represented by at least 3 pixels in the horizontal axes. Thus it is possible to calculate the maximum flight height based on the resolution of 40/3 = 13,3 cm/pixel.

As we can see from the graphic above, with the UAV flying at 55 meters high, it will meet the horizontal pixel size requirement.

Therefore, once the minimum and maximum flight height is defined, we can consider this range as valid and refine the optimal flight height based on other requirements of interest, such as, for example, the overlap and the maximum allowable lateral displacement of the harvester.

Figure 32 – *Pixel* resolution size

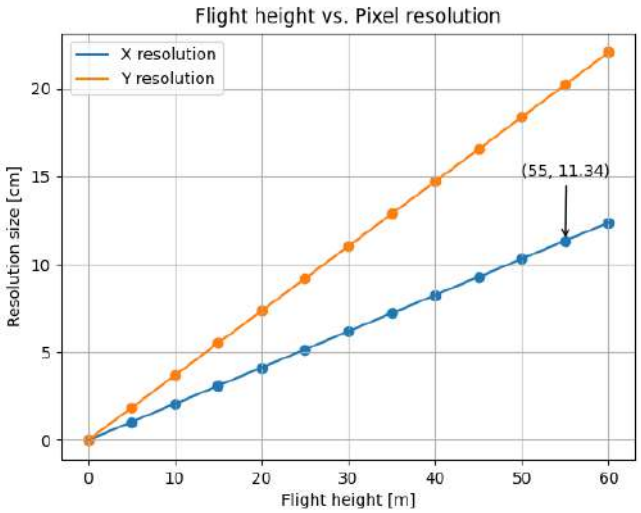

Source: Author.

4.6.4 Maximum time processing

In order to define the maximum processing time that each image can consume to enable the algorithm for the application, a mathematical modeling was developed based on the application requirements. The main restriction for this application is the speed of the harvester, which is stipulated at up to 6 km/h in conditions where the terrain is favorable. It is assumed that the speed of the UAV will be the same as that of the combine. Another input parameter that does not allow adjustments is the field of view of the camera used, fixed at 70°. The input parameter 'overlap' means in percentage the pixel correspondence between a new image and the previous image. The literature indicates that more than 80% overlap is considered optimal for computer vision-based trajectory control applications. This parameter can be adjusted in this range of 80 to 95 according to application interests. Greater overlap brings greater reliability to the combine path, but requires processing to be done in a timely manner. Finally, the parameter that we can adjust according to our needs is the height of the drone. The higher the drone height, given the same overlap factor, the longer there is to process an image before a new one queues to be processed.

Also, the higher the UAV, the greater the coverage area per image, increasing the likelihood that the image will contain several different sugarcane elements or even cut lines will appear as they follow the curves. level related to the terrain topology. On the other hand, the lower the height of the UAV, the lower the number of cut lines present in the image. This causes the algorithm to have little reliability in the final result, in addition to the noise present in the image having great relevance, bringing inaccuracy.

Figure 33 – fps processing vs drone height

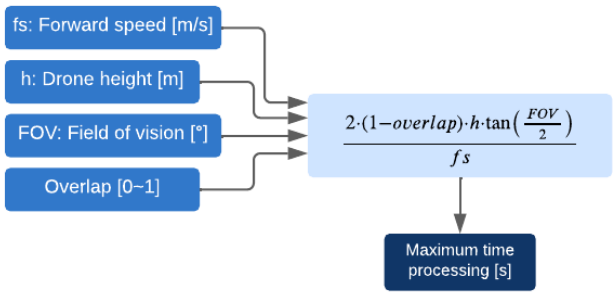

Source: Author.

Figure 34 – fps processing vs drone height

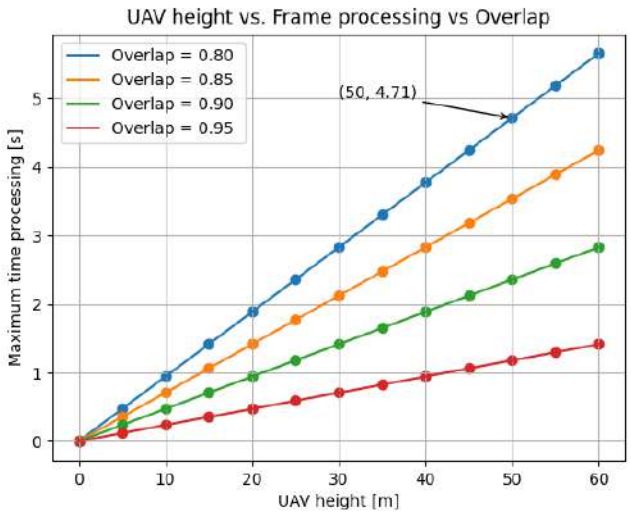

Source: Author.

4.6.5 Maximum lateral displacement

Once theoretically calculated the minimum and maximum height suitable for the application, we will analyze the relationship between the accuracy of the orientation angle detected with the lateral advance of the harvester. The more imprecise the result of the algorithm, the greater the advance of the harvester in the neighboring planting lines, causing kneading, something we want to avoid at all costs. One way to mitigate the risk of wrinkling given a sporadic inaccuracy of the algorithm is to reduce the detection time, that is, to reduce the processing time of each image.

4.6.6 Requirements summary

- ❏ Maximum flight high: 25 meters.
- ❏ Minimum flight high: 55 meters.

Figure 35 – Effects of MAE

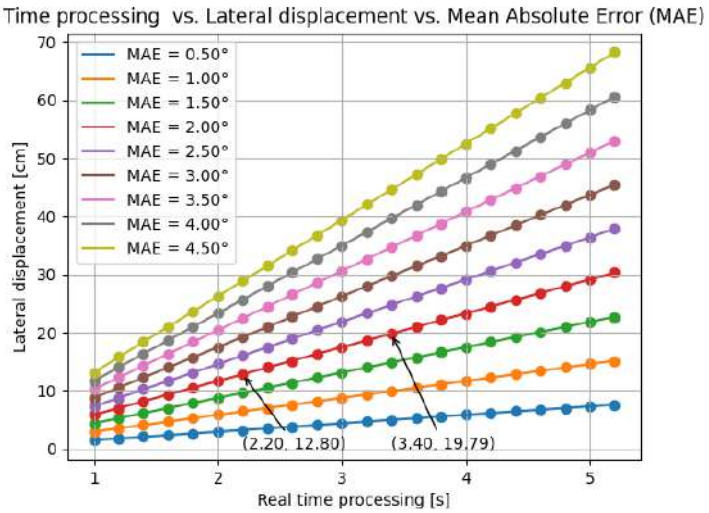

Source: Author.

- ❏ Maximum image processing time: 4.71 seconds
- ❏ Maximum lateral displacement: 10 centimeters.

Chapter 5

Experimental Results

5.1 Experimental Setup

For the proposed tests of crop row orientation detection, it was evaluated 40 images selected by an specialist where the ground truth of the cutting line orientation was determined by a manual system based on overlapping bars on the cutting line with referenced angles.

For the experiments data analysis, we defined two criteria: the median angular error along with its interquartile range (IQR) and the image processing time, as precision and processing time are essential for the success of the method.

The table 1 describes the hardware and software specification where the application was evaluated.

Table 1 – Hardware and software description.

Processor	Intel® Core™ i5-4200U CPU @ 1.60GHz
Graphics	Mesa DRI Intel® HD Graphics 4400
RAM memory	8 GB
Operational System	Linux 5.10.42-1-MANJARO
Python Version	Python 3.9.5
OpenCV library	4.5.2

5.2 Ground Truth Measurements

With the combined expert's labeling which generated an average angle and standard deviation for each image of our dataset was possible to compare both heuristics created

as well as possible to indicate if an image was marked as appropriate to be used as ground truth or not.

Over the 40 images selected for composition of the data set, four of them were discarded according to the methodology used to generate the ground truth. The figure below shows the figures that had a high standard deviation in the experts' scores.

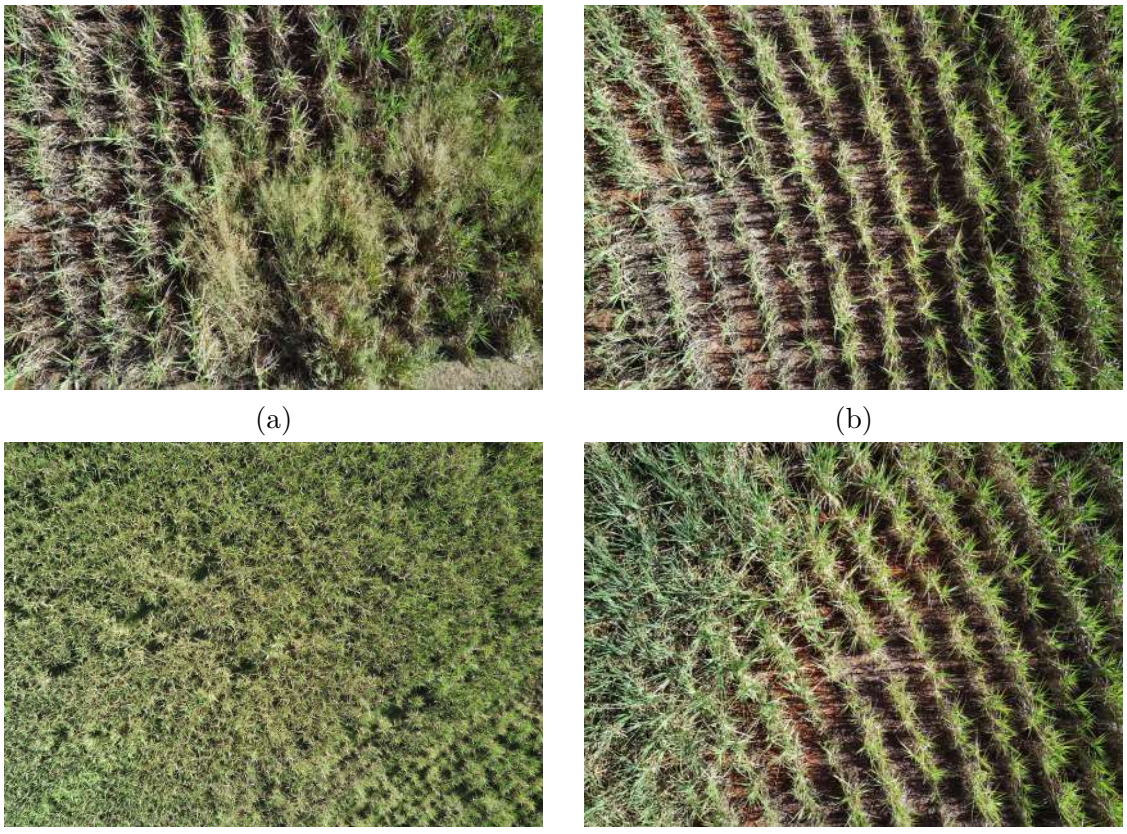

(a) (b)

(c) (d)

Figure 36 – Vertical projection algorithm steps: (a) and (c) image rotated in specific angle; (b) and (d) respective vertical projection curves

Looking at the image in the figure 36(a), we see that there is a high area of weeds in the center of the image and the visible crop lines are in terrain with irregular geometry. In Figure 36(b) and (d) the planting lines follow the contours of the terrain in a curve. Differently, Figure 36(c) shows an image of sugarcane taken from a higher altitude than the others and where the perception of crop lines is compromised due to the high density of vegetation in the area.

Therefore, these 4 images are inappropriate to be used as absolute truth in the results that will be shown below. The dataset then has 36 qualified images to carry out the comparative analysis with the results of the experts.

5.3 Heuristic based on column projections

Applying our heuristic process to all images of our data set classified by the experts, returned to us the results described below. The images present in figure 37 are very interesting and deserve to have a particular algorithm performance analyses.

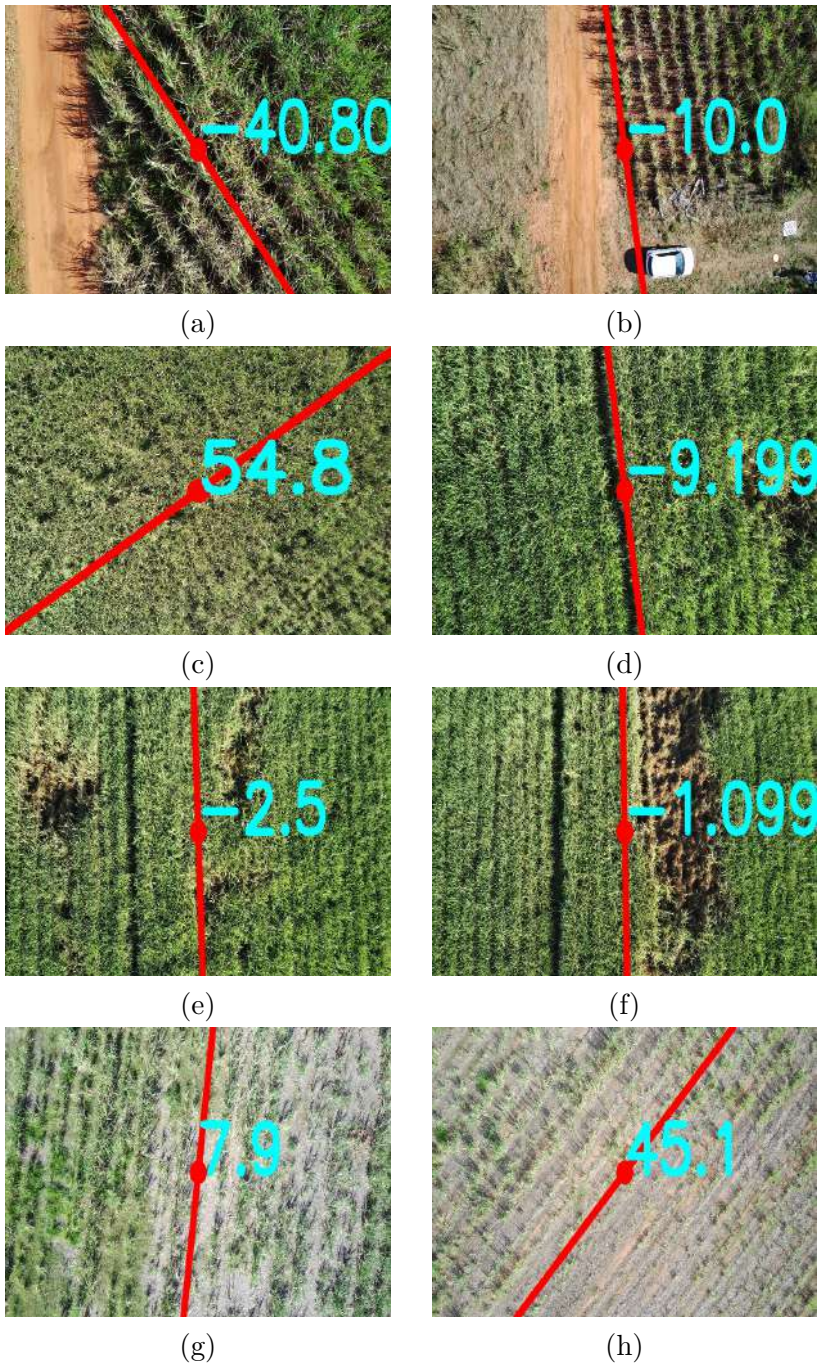

(a) (b) (c) (d) (e) (f) (g) (h)

Figure 37 – Angle orientations detected at crop row images with: (a) an off-road, (b) an off-road and a car, (c) high sugarcane density (d) weed region on the right side, (e) weed region at both sides, (f) a big weed area, (g) very constrast variation and (h) low sugarcane density.

❑ Figure (a): There is an off-road line at the edge of the plantations which does not

pose a challenge for the algorithm to correctly detect the orientation angle;

- ❏ Figure (b): Only one quarter of the image area are crop lines. There are three different kind of noise: An off-road, a car and non-sugarcane area;
- ❏ Figure (c): There is an area of high density sugarcane where the algorithm can find a good orientation result;
- ❏ Figure (d): There is a small weed area on the right side;
- ❏ Figure (e): There is a small weed area on both side;
- ❏ Figure (f): There is a relevant part of the image with an area of weeds, around 20%. This shows the robustness of the algorithm in dealing with this scenario;
- ❏ Figure (g): Here there is high color variation compared with other images on the data set;
- ❏ Figure (h): The algorithm was able to correctly detect the orientation angle even in a low sugarcane density scenario.

Below, we investigate the impact of of Savitzky-Golay window size, scan resolution angle and quarter and half image resolution in terms of image processing time and crop row orientation angle accuracy. Tables 2, 4, and 3 present the summary of results. In figure 38 there are two box plot graph for mean absolute error data of the detected angles between the algorithm and the experts' results. A full factorial design was carried out, selecting as factors, the Savitzky-Golay window size (7, 15 and 23), resolution step (0.1° and 1°) and image resizing (quarter resolution and half resolution). The description of the configurations present on the legend of the figure 38 are below:

- ❏ 01 and 1 before letter. Means 0.1 and 1 degrees for scan angle resolution;
- ❏ H and Q after scan angle resolution: Means half and quarter resize of original image resolution respectively;
- ❏ 7, 15 and 23 after image resolutions: Means the size in pixel of window parameter for Savitzky-Golay filter.

Table 2 – Average processing time for the different heuristic settings

Image processing time						
Scan Angle Resolution	**0.1**			**1**		
Windows size [pixel]	**7**	**15**	**23**	**7**	**15**	**23**
One-quarter Image processing time [s]	6.555	6.514	8.289	0.871	1.017	0.867
One-half Image processing time [s]	21.78	20.176	20.889	2.221	2.155	2.164

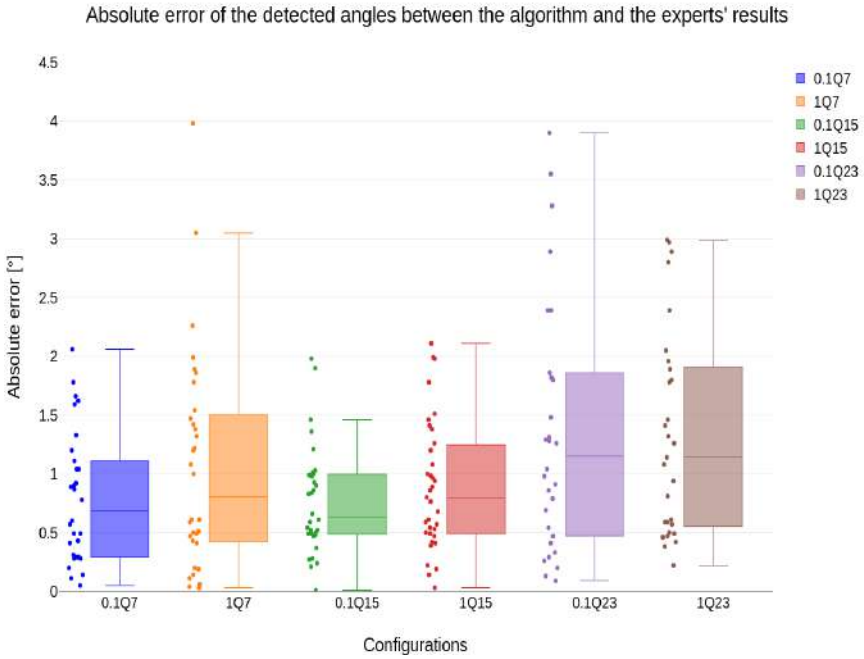

(a)

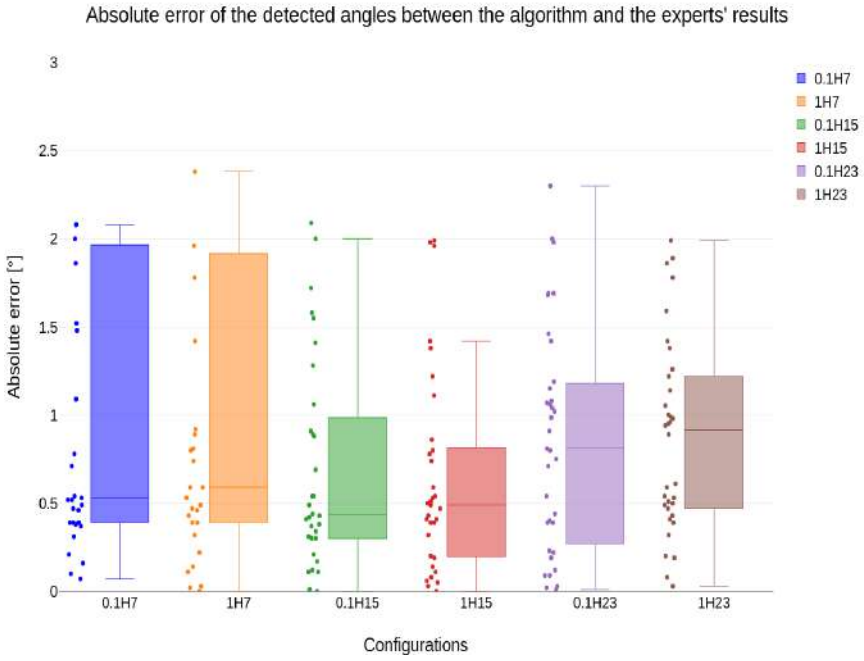

(b)

Figure 38 – (a) Box plot of absolute angle errors for factors Savitzky-Golay window (7, 15, 23) and resolution step (0.1° and 1°) for image in quarter resolution (b) Box plot of absolute angle errors for factors Savitzky-Golay window (7, 15, 23) and resolution step (0.1° and 1°) for image in half resolution

We can highlights some of important results in terms of interquartile, outliers, data distribution and time processing for all results sets:

- 01Q15 has the minimum interquartile range: 0.51°. 01H7 has the maximum: 1.54°;
- 1H15 has the minimum MAE is 0.64° and 01H7 the maximum: 5.63°.
- 1Q23 has the maximum amount of outliers: 7 in a 36 samples
- 1Q23 has the maximum outlier value: 86.54°.
- 1Q15 has only one outlier of 4.05°.
- 1Q15 has the minimal difference between mean and median and is potentially symmetrical by Skewness measured value;
- 1Q15 has is normal like tails by Excess Kurtosis;
- In table 5 we can see the minimum amount of time was to process 1Q7 and the maximum to process 0.1H7 configuration as expected.

Table 3 – Trials results comparison with one half of the original image resolution

Groups:	**0.1H7**	**1H7**	**0.1H15**	**1H15**	**0.1H23**	**1H23**
Sample size (n):	31	31	32	33	35	34
Minimum:	0.07	0	0	0	0.01	0.03
Q1:	0.39	0.39	0.3	0.2	0.31	0.47
Median:	0.53	0.59	0.435	0.49	0.81	0.915
Q3:	1.93	1.87	0.985	0.8	1.17	1.22
Maximum:	47.99	44.49	2.09	1.99	2.3	1.99
Mean ($\bar{x}$):	5.64	5.48	0.69	0.64	0.86	0.87
Skewness:	2.47	2.34	1.02	1.22	0.47	0.50
Skewness Shape:	Asymmetrical, right/positive (pval=0)	Asymmetrical, right/positive (pval=0)	Asymmetrical, right/positive (pval=0.014)	Asymmetrical, right/positive pval=0.003)	Potentially Symmetrical (pval=0.238)	Potentially Symmetrical (pval=0.213)
Excess kurtosis:	5.95	4.99	-0.02	0.76	-0.64	-0.62
Tails Shape:	Leptokurtic, long heavy tails (pval=0)	Leptokurtic, long heavy tails (pval=0)	Potentially Mesokurtic, normal like tails (pval=0.982)	Potentially Mesokurtic, normal like tails (pval=0.339)	Potentially Mesokurtic, normal like tails (pval=0.414)	Potentially Mesokurtic, normal like tails (pval=0.433)
Outliers:	50.34, 82.3, 64, 63.49, 61.21	50.54, 87.5, 62.2, 63.59, 61.01	68.46, 52.65, 4.21, 14.22	68.46, 2.63, 11.472	5.56	5.46, 2.8

Table 4 – Trials results comparison with one quarter of the original image resolution

Groups:	**0.1Q7**	**1Q7**	**0.1Q15**	**1Q15**	**0.1Q23**	**1Q23**
Sample size (n):	30.00	32.00	32.00	35.00	30.00	29.00
Minimum:	0.05	0.03	0.01	0.03	0.09	0.22
Q1:	0.29	0.42	0.49	0.50	0.47	0.57
Median:	0.69	0.81	0.64	0.80	1.15	1.14
Q3:	1.11	1.51	1.00	1.23	1.86	1.89
Maximum:	2.06	3.98	1.98	2.11	7.56	2.99
Mean ($\bar{x}$):	0.79	1.06	0.77	0.89	1.53	1.32
Skewness:	0.65	1.29	0.97	0.66	2.30	0.67
Skewness Shape:	Potentially Symmetrical (pval=0.128)	Asymmetrical, right/positive (pval=0.002)	Asymmetrical, right/positive (pval=0.02)	Potentially Symmetrical (pval=0.095)	Asymmetrical, right/positive (pval=0)	Potentially Symmetrical (pval=0.125)
Excess kurtosis:	-0.54	2.03	0.98	-0.28	7.07	-0.76
Tails Shape:	Potentially Mesokurtic, normal like tails (pval=0.516)	Leptokurtic, long heavy tails (pval=0.012)	Potentially Mesokurtic, normal like tails (pval=0.224)	Potentially Mesokurtic, normal like tails (pval=0.724)	Leptokurtic, long heavy tails (pval=0)	Potentially Mesokurtic, normal like tails (pval=0.369)
Outliers:	58.74, 56.25, 66.09, 3.98, 6.141, 16.929	66.54, 66.59, 4.911, 15.439	3.15, 2.09, 4.51, 2.68	4.05	19.39, 11.02, 86.54, 50.1, 51.44, 18.217	19.49, 11.02, 86.54, 50, 51.14, 7.542, 18.185

The best Configuration and Fulfillment of Requirements

As we cannot see that small scan angle resolution like 0.1° doesn't results in a much better performance metrics compared with 1° and the time processing increase is relevant, we will just to discard it. Also, we will restrict our selection only at configurations classified as potentially symmetrical. Our filter selected 1Q15, 1Q23 and 1H23 configurations. Looking for the lowest MAE and time processing we can see that 1Q15 can be choose as the best configuration: MAE (0.890°) and process time (1.017 s). The time processing should be be carefully considered here because its value is platform-dependent, which means that this time can change depending of hardware capabilities. Finally, we can take MAE and time values as input for find out the theoretical lateral displacement showed in figure 35. The summary of the parameters and theoretical values of the best parameters for orientation angle detection based on radon transform can fulfill the requirements.

- ❏ One-quarter of original crop row image;
- ❏ Algorithm scan angle resolution (1°);
- ❏ Mean absolute error (normal distributed): (0.890°) degrees
- ❏ Time processing: (1.017 s);
- ❏ Lateral displacement: < 3cm.

5.4 Heuristic based on Radon Transform

Applying the process to find orientation based on Radon Transform Algorithm described in Methodology chapter to all of our data set images results in the results described below. The images present in figure 39 are very interesting and deserve to have a particular algorithm performance analyses.

- ❏ Figure (a): There is an off-road line at the edge of the plantations which does not pose a challenge for the algorithm to correctly detect the orientation angle;
- ❏ Figure (b): Only one quarter of the image area are crop lines. There are three different kind of noise: An off-road, a car and non-sugarcane area;
- ❏ Figure (c): There is a high density sugarcane area where the algorithm couldn't find a good orientation result;
- ❏ Figure (d): There is a small weed area on the right side;
- ❏ Figure (e): There is a small weed area on both side;

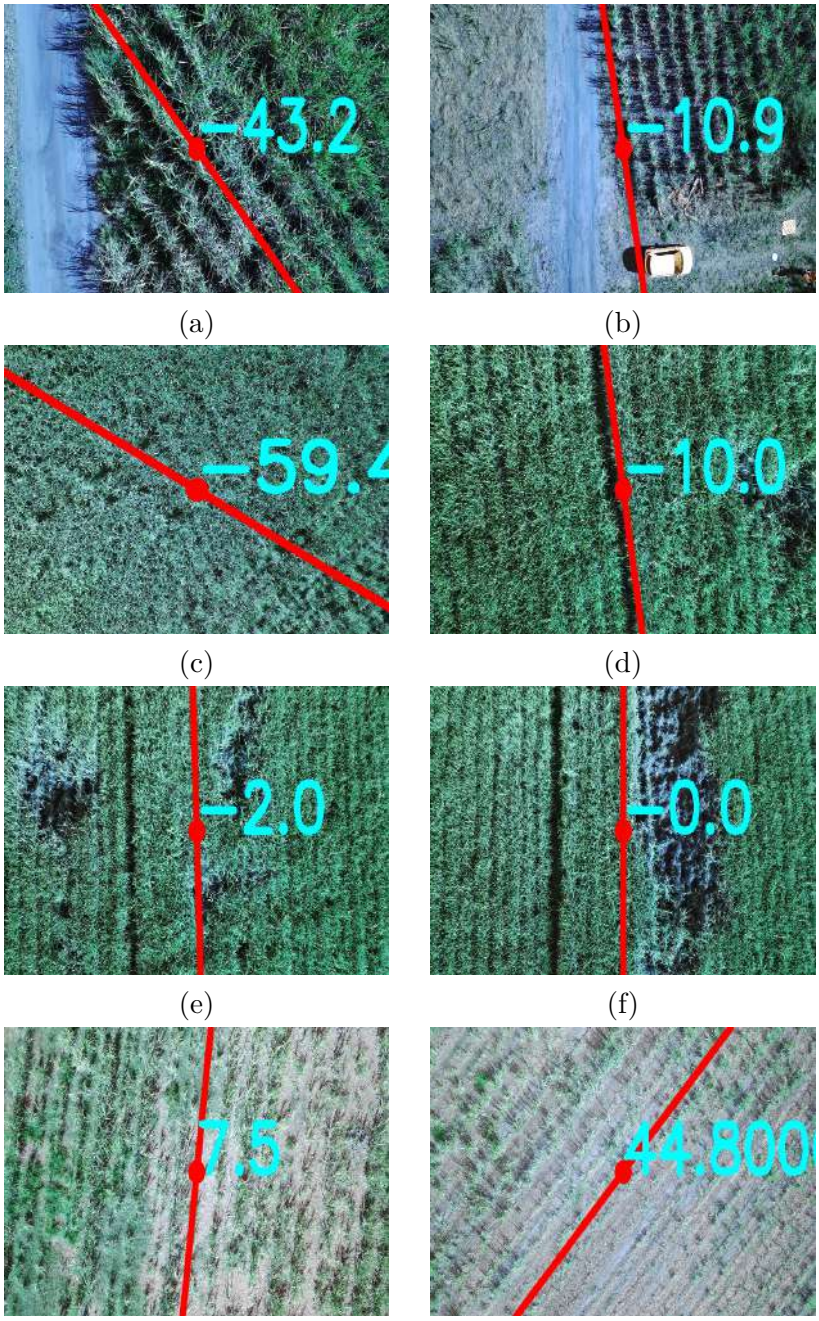

(a) (b) (c) (d) (e) (f) (g) (h)

Figure 39 – Angle orientations detected at crop row images with: (a) an off-road, (b) an off-road and a car, (c) high sugarcane density (d) weed region on the right side, (e) weed region at both sides, (f) a big weed area, (g) very contrast variation and (h) low sugarcane density.

- ❏ Figure (f): There is a relevant part of the image with an area of weeds, around 20%. This shows the robustness of the algorithm in dealing with this scenario;
- ❏ Figure (g): Here there is high color variation compared with other images on the data set;
- ❏ Figure (h): The algorithm was able to correctly detect the orientation angle even

in a low sugarcane density scenario.

In order to get a overall statistical analyses of the algorithm performance compared with expert´s results, the box plot of the figure 40 shows graphically the locality, spread and skewness groups of mean absolute error data through their quartiles. The box plot shows six different test results with different settings.

Basically, the different settings used is the resize of the original crop row image resolution and the scan angle resolution used by algorithm to rotate the image to take the projections intensity sum. The tests were performed with one-quarter and one-half of resolution and scan angle resolution of 0.1°, 0.5° and 1° degrees and then performing a full factorial analyses between them. The description of the configurations present on the legend of the figure 40 are below:

- ❏ 01.H is scan resolution of 0.1 degrees for a one half of original image resolution;
- ❏ 01.Q is scan resolution of 0.1 degrees for a one quarter of original image resolution;
- ❏ 05.H is scan resolution of 0.5 degrees for a one half of original image resolution;
- ❏ 05.Q is scan resolution of 0.5 degrees for a one quarter of original image resolution;
- ❏ 1.H is scan resolution of 1 degrees for a one half of original image resolution;
- ❏ 1.Q is scan resolution of 1 degrees for a one quarter of original image resolution.

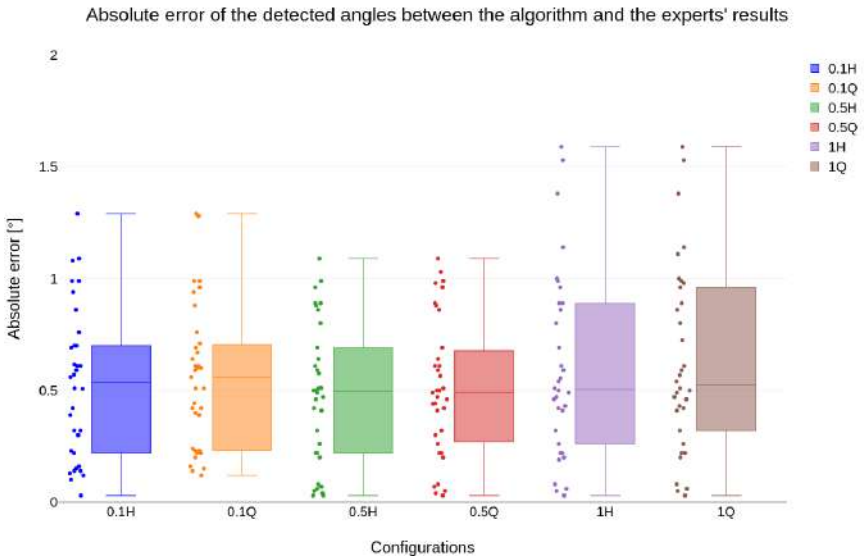

Figure 40 – Box plot of absolute angle errors for image resolution (half and one-quarter) and scan angle resolution (0.1° and 1°) factors.

All associated statistical results of the box plot of figure 40 are in the table of 5 and 6.

Table 5 – Average image process time - Radon algorithm

Image processing time			
Scan Angle Resolution	**0.5**	**1**	**0.1**
One-quarter Image processing time [s]	1.569	0.800	6.412
One-half Image processing time [s]	5.527	2.910	26.847

Table 6 – Radon Algorithm trials results comparison with one quarter and one half of the original image resolution

Groups:	**0.1H**	**0.1Q**	**0.5H**	**0.5Q**	**1H**	**1Q**
Sample size (n):	34.00	35.00	34.00	35.00	34.00	34.00
Minimum:	0.03	0.12	0.03	0.03	0.03	0.03
Q1:	0.22	0.24	0.22	0.28	0.26	0.32
Median:	0.54	0.56	0.50	0.49	0.51	0.53
Q3:	0.70	0.70	0.69	0.67	0.89	0.96
Maximum:	1.29	1.29	1.09	1.09	1.59	1.59
Mean ($\bar{x}$):	0.52	0.55	0.48	0.51	0.60	0.63
Skewness:	0.43	0.60	0.15	0.24	0.78	0.62
Skewness Shape:	Potentially Symmetrical (pval=0.284)	Potentially Symmetrical (pval=0.13)	Potentially Symmetrical (pval=0.701)	Potentially Symmetrical (pval=0.554)	Potentially Symmetrical (pval=0.054)	Potentially Symmetrical (pval=0.127)
Excess kurtosis:	-0.69	-0.18	-0.99	-0.80	0.11	-0.22
Tails Shape:	Potentially Mesokurtic, normal like tails (pval=0.378)	Potentially Mesokurtic, normal like tails (pval=0.82)	Potentially Mesokurtic, normal like tails (pval=0.207)	Potentially Mesokurtic, normal like tails (pval=0.301)	Potentially Mesokurtic, normal like tails (pval=0.887)	Potentially Mesokurtic, normal like tails (pval=0.779)
Outliers:	2.39, 1.88	2.39	2.39, 1.98	2.39	2.39, 1.98	2.39, 2.19

We can highlights some of important results in terms of interquartile, outliers, data distribution and time processing for all results sets:

- ❏ All of the median and mean is close each other and near to 0.5° of mean absolute error (MAE);
- ❏ The minimum interquartile range is 0.385 and the maximum is 0.64;
- ❏ The maximum MAE is 1.59°;
- ❏ The maximum amount of outliers is two in a 34 samples;
- ❏ The maximum outlier value is 2.39°;
- ❏ All tests are potentially symmetrical by Skewness measured value;
- ❏ All test are normal like tails by Excess Kurtosis;
- ❏ In table 5 we can see the minimum amount of time was to process 1Q and the maximum at 0.1H configuration as expected.

The best Configuration and Fulfillment of Requirements

As we cannot see that small scan angle resolution like 0.1° doesn't results in a much better performance metrics compared with 0.5° and 1 1°, we will just to discard it. Also, as all results was classified as potentially symmetrical, to select the best configurations we can looking for the lowest MAE and time processing. We can see that 0.5Q can be choose as the best configuration: MAE (0.510°) and process time (1.569 s). The time processing should be carefully considered here because its value is platform-dependent, which means that this time can change depending of hardware capabilities. Finally, we can take MAE and time values as input for find out the theoretical lateral displacement showed in figure 35. The summary of the parameters and theoretical values of the best parameters for orientation angle detection based on radon transform that can fulfill the requirements are:

- ❏ One-quarter of original crop row image;
- ❏ Algorithm scan angle resolution (0.5°);
- ❏ Mean absolute error (normal distributed): (0.510°) degrees
- ❏ Time processing: (1.569 s);
- ❏ Lateral displacement: < 3cm.

5.5 Comparison of approaches

In terms of meet requirements both approach can achieve with large advantages of critical values for timing and accuracy which enables these algorithms to detect crop row orientations from aerial images in real-time operations. When comparing the results obtained by both approach can be observed that considering the same scenario - the same application and same hardware - there is a trade-off between higher image resolution and rotation resolution angle. The higher the image resolution, the longer the processing time and accuracy. The larger the rotation resolution angle, the lower processing time and accuracy.

To assess the average running time for both heuristics, the same common parameter settings were applied for 50 iterations. As shown in figure 41 the execution time is not far off, with the projection heuristic averaging 0.818 ± 0.008 and the Radon heuristic 0.796 ± 0.026 seconds.

To determine whether two normal distributions are equivalent, a common method is to use a two-sample t-test. This test compares the means of the two distributions and calculates a t-value and a p-value. If the p-value is less than a certain threshold (for example, 0.05), this suggests that the means of the two distributions are statistically different, indicating that the distributions are not equivalent.

To simplify our analysis, we will skip the normal distribution characterization test and apply the two-sample t-test directly. This results in a t-statistic value of 5.555 and a p-value of $2.379e-07$. As the p-value is less than a significance level of 5%, the null hypothesis is validated, which means that these two samples are not equal and so we can say that the Radon heuristic is slightly faster than the projection.

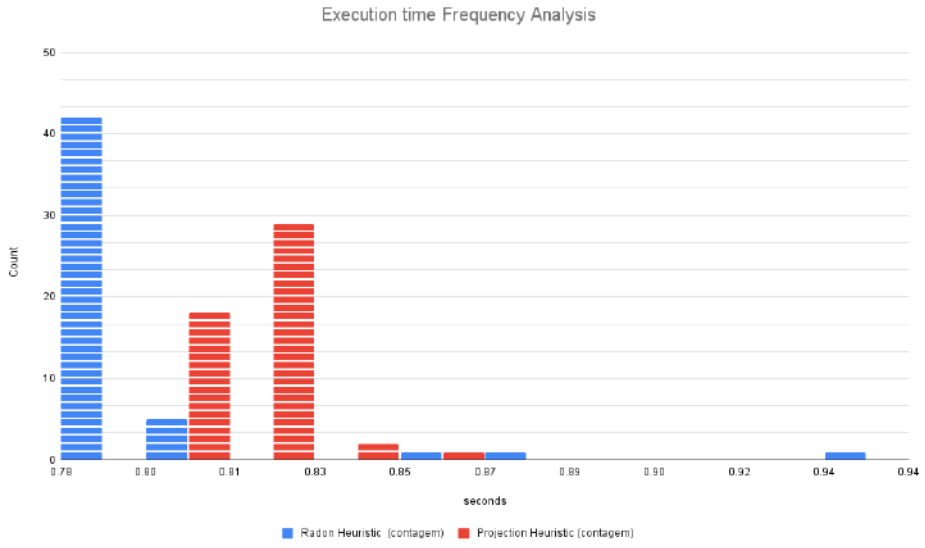

Figure 41 – Frequency analysis for execution time with one-quarter resolution and scan angle resolution of 1°.

As it can be observed for crop row detection based on vertical projection pixel intensity accumulation algorithm, neither window size nor step resolution or image size changed the median significantly, all of the tests were around 0.75°, with the outliers removed. The configurations for a quarter image resolution, window size of 15 were the only configurations that did not raised outliers in the errors, being able to classify even the most difficult scenarios. In the other direction, the configurations for half image resolution, window size 7, had a really large interquartile range (IQR) and a high number of outliers, being dependent of the type of image. The main problem for the method of tree segmentation using Excess Green Index is the presence of weeds and other green objects, which are mixed with the trees of the crop and makes impossible to distinguish the crop.

For crop row angle orientation detection based on Radon Transform Algorithm, neither scan angle resolution or image size changed the median significantly, all of the tests were around 0.52°, with the outliers removed. Image size and resolution did not have much effect on the final result, being the best result the configuration of 1/4 of the original image resolution. The scan angle of 0.5 degree resolution can perform balanced results in terms of timing and accuracy.

The second approach generated much less outliers compared with Algorithm based on vertical projection pixel intensity accumulation algorithm. From a total of 36 samples, the Radon Transform based Algorithm generated a maximum of 2 in the worst case, with a value of 2.36 degrees. The first heuristics generated 7 outliers in the worst case with values up to 87 degrees of error. In this respect, the Radon approach is more reliable than the vertical projections with filtered variance. Not least, all configurations tested with radon generated confirmed normal distributions with excess kurtosis value and skewness. Differently, most of the configurations used in the vertical projection algorithm generated asymmetric distributions.

From the images marked as outliers, it was observed that, if the sugarcane was too dense, given a fix morphological operation kernel, the soil points were filtered out raising the angle error. When the soil points vanish, the proposed method can not detect any line.

Overall, after analyzing the performance for all scenarios, it can be concluded that the proposed crop row orientation, using the Radon based algorithm, kept its high accuracy even for a different topology of the system. Therefore, the proposed crop row orientation is more reliable in comparison with the other crop row orientation detectors, considering that the system can change its topology, as in a condition of different angle lines, for example. The proposed method also proved to be robust in angle estimation despite the presence of punctual faults, caused by crushing or weeds (see Fig. 37b).

Chapter 6

Conclusion

Our proposal, a heuristic based on vertical projection pixel intensity accumulation using only the vegetative index (ExG), morphological operations, and rotations accompanied by column projections proved to be able to find the average orientation angle of the average crop lines. Besides that, the use of the Savitzky-Golay filter of second order for the first derivative proved to be efficient in finding the points of higher variation in the projection vector. A suitable configuration was found from a factorial test, reaching a median absolute error of 0.890° and IQR of 0.735° with processing time of 1.017 seconds.

A second heuristic was created to compare our approach with the recent state-of-the-art strategies. By using only the decreased mean from gray-scale image processing techniques before applying into a Radon transform. A posterior intensity absolute average filter to find the Crop row angle orientation. The results show that the proposed reproduced methodology was able to detect the crop rows orientation angle with a median absolute error of 0.51° and IQR of just 0.385° with processing time of 1.569 seconds. Even by changing a few configurations, difficult scenarios were able to be identified given a high accuracy angle estimation.

Moreover, both proposed methods in the above mentioned configuration was able to estimate the sugarcane orientation, despite a dense plantation, street presence and weed and plantation faults. Other advantages in relation to the state of the art are the ability to detect cut lines in RGB images acquired by the low-cost UAV orthogonal imaging system in low-altitude flights, without orthorectification or learning-based steps that result in simple implementation and low computational cost.

However, from the analysis of the results generated by the methodology designed to generate the absolute truth of the experts, the relief of the terrain and the distortion errors caused by the camera lens can negatively influence the performance of the algorithm.

However, these adverse effects are mitigated by maintaining a low flight height, that is, less than 50 meters in our case.

The contributions of this work are a bank of aerial images of labelled sugarcane plantations, a method for fusing the knowledge of experts using the Kalman Filter and a heuristic for estimating plantation line angles. The generated database has a diversity of location, time, plantation quality and growth stage. The normality analysis from the experts labeling proved to be an essential point for using the Kalman Filter to perform the fusion of the labeling, creating an accurate background with a standard deviation smaller than just one expert label.

Moreover, extracting features from images of unstructured environments, such as sugarcane fields, can be a challenging task due to several factors. One major challenge is the complexity of the environment, as the images often contain a large number of objects with different shapes, sizes, and colors. This makes it difficult to differentiate between important features, such as the sugarcane plants, and the surrounding vegetation, rocks, and other clutter.

Another challenge is the variability in the images, as the lighting conditions, camera angle, and other factors can significantly impact the appearance of the environment. This can make it difficult to extract consistent and accurate features, as well as to generalize the results to other images.

Additionally, the large scale of the images can also pose a challenge, as it may not be feasible to manually annotate all of the important features in the image. Automated feature extraction algorithms may also struggle with the high degree of variability in the images, leading to sub optimal results.

To overcome these challenges, it is necessary to employ advanced image processing techniques, such as deep learning and computer vision algorithms, to extract meaningful features from the images. These algorithms can be trained on annotated images to learn how to identify important features, such as the sugarcane plants, and to filter out the clutter. However, these algorithms also require large amounts of data to train and validate their results, which can be a significant challenge in itself.

We intend to improve this approach by removing objects, such as roads and trees, in future work. The image base should be reanalysed, with more markings for unwanted objects. In addition, more conditions and locations can be added to complement the bank, which will bring more robustness to the algorithms.

Finally, this work represents a significant milestone for our research group, as it marks the first study of its kind to be conducted within our organization. This study has produced a wealth of results that have the potential to be explored in much greater detail by future researchers. Whether through further study, or by applying these results in new and innovative ways, there is great potential for future research to make a significant impact in this field.

6.1 Publications

A conference paper from this work was published at the 18th IEEE Latin American Robotics Symposium 2021 (LARS). https://ieeexplore.ieee.org/document/9605401.

Bibliography

AERONAVES não tripulada se o acesso ao espaço aéreo brasileiro. 2019. <https://publicacoes.decea.mil.br/api//storage/uploads/files/75a09bfd-5e5d-4f9a-b4485ccd3fd4627a.pdf>. Accessed: 2021-9-2.

AMARASINGAM, N. et al. A review of UAV platforms, sensors, and applications for monitoring of sugarcane crops. **Remote Sensing Applications: Society and Environment**, v. 26, p. 100712, abr. 2022. ISSN 2352-9385.

BAH, M. D.; HAFIANE, A.; CANALS, R. Deep learning with unsupervised data labeling for weed detection in line crops in uav images. **Remote Sensing**, v. 10, n. 11, 2018. ISSN 2072-4292.

BALAFOUTIS, A. et al. Precision agriculture technologies positively contributing to GHG emissions mitigation, farm productivity and economics. **Sustain. Sci. Pract. Policy**, Multidisciplinary Digital Publishing Institute, v. 9, n. 8, p. 1339, jul. 2017.

BASSO, M. A framework for autonomous mission and guidance control of unmanned aerial vehicles based on computer vision techniques. **Universidade Federal do Rio Grande do Sul, Porto Alegre**, 2018.

CAI, H. et al. A new iterative triclass thresholding technique in image segmentation. **IEEE Transactions on Image Processing**, v. 23, n. 3, p. 1038–1046, 2014.

CARDOSO, L. A. S.; FARIAS, P. R. S.; SOARES, J. A. C. Use of unmanned aerial vehicle in sugarcane cultivation in brazil: A review. **Sugar Tech**, abr. 2022. ISSN 0974-0740.

CELADES-MARTíNEZ, J. A. et al. A technique to evaluate field traffic patterns of sugarcane harvester using autopilot system. In: **2020 IEEE Colombian Conference on Communications and Computing (COLCOM)**. [S.l.: s.n.], 2020. p. 1–6.

CONAB. Acompanhamento da safra brasileira de cana-de-açucar. **Companhia Nacional de Abastecimento**, 2021.

CUNHA, L. S. da. **Assimetria e Curtose**. 2017. Disponível em <http://www.uel.br/pessoal/lscunha/pages/arquivos/uel/Economia%20Noturno/Aula%206%20-%20Assimetria%20e%20Curtose.pdf>. Acesso em 18 setembro 2021.

DIAS, L. V. A. **Estudo e análise de diferentes métodos de calibração de câmeras**. Dissertação (Mestrado) — universidade tecnológica federal do paraná, 2015.

EMBRAPA. **Visão 2030: O futuro da agricultura brasileira**. [S.l.: s.n.], 2018.

FILHO, O. M.; NETO, H. V. **Processamento Digital de Imagens**. [S.l.]: Brasport, 1999.

FIMI X8 SE. 2021. Disponível em <https://www.fimi.com/fimi-x8-se.html>. Acesso em 01 setembro 2021.

GARCÍA-SANTILLÁN, I. D. et al. Automatic detection of curved and straight crop rows from images in maize fields. **Biosystems Eng.**, v. 156, p. 61–79, abr. 2017. ISSN 1537-5110.

GARCíA-SANTILLáN, I. D.; PAJARES, G. On-line crop/weed discrimination through the mahalanobis distance from images in maize fields. **Biosystems Engineering**, v. 166, p. 28–43, 2018. ISSN 1537-5110.

GIERNACKI, W.; GOSLINSKI, J.; ESPINOZA-FRAIRE, T. Mathematical modeling of the coaxial quadrotor dynamics for its attitude and altitude control. **Energies**, v. 14, 02 2021.

GUERRERO, J. et al. Support vector machines for crop/weeds identification in maize fields. **Expert Systems with Applications**, v. 39, n. 12, p. 11149–11155, 2012. ISSN 0957-4174.

HAMUDA, E.; GLAVIN, M.; JONES, E. A survey of image processing techniques for plant extraction and segmentation in the field. **Comput. Electron. Agric.**, v. 125, p. 184–199, jul. 2016.

HASSANEIN, M.; KHEDR, M.; EL-SHEIMY, N. Crop row detection procedure using low-cost uav imagery system. **The International Archives of the Photogrammetry, Remote Sensing and Spatial Information Sciences**, XLII-2/W13, p. 349–356, 2019.

HOUGH, P. **Method and means for recognizing complex patterns**. U.S. Patent 3 069 654, Dec. 1962.

IGLEWICZ, B.; HOAGLIN, D. **How to Detect and Handle Outliers**. ASQC Quality Press, 1993. (ASQC basic references in quality control). ISBN 9780873892476. Disponível em: <https://books.google.com.br/books?id=siInAQAAIAAJ>.

JÚNIOR, M. R. B. et al. Mapping gaps in sugarcane by UAV RGB imagery: The lower and earlier the flight, the more accurate. **Agronomy**, v. 11, n. 12, dez. 2021.

KITAHARA, J. R. **Quora**. 2021. Disponível em <https://www.quora.com/Is-it-a-normal-probability-distribution-that-has-a-mean-%CE%BC-0-and-a-standard-deviation-%CF%83-1>. Acesso em 03 outubro 2021.

KRüGER, G.; SPRINGER, R.; LECHNER, W. Global navigation satellite systems (gnss). **Computers and Electronics in Agriculture**, v. 11, n. 1, p. 3–21, 1994. ISSN 0168-1699. Global Positioning Systems in Agriculture.

KULBACKI, M. et al. Survey of drones for agriculture automation from planting to harvest. In: . [S.l.]: IEEE, 2018.

LARIVE, C. K.; SWEEDLER, J. V. Celebrating the 75th anniversary of the acs division of analytical chemistry: A special collection of the most highly cited analytical chemistry papers published between 1938 and 2012. **Analytical Chemistry**, v. 85, n. 9, p. 4201–4202, 2013. PMID: 23647149. Disponível em: <https://doi.org/10.1021/ac401048d>.

MALDANER, L. F. et al. Identification and measurement of gaps within sugarcane rows for site-specific management: Comparing different sensor-based approaches. **Biosystems Eng.**, v. 209, p. 64–73, set. 2021. ISSN 1537-5110.

MEYER, G. E.; HINDMAN, T.; LAKSMI, K. Machine vision detection parameters for plant species identification. **Precision Agriculture and Biological Quality**, v. 3543, nov. 1998.

MEYER, G. E.; NETO, J. C. Verification of color vegetation indices for automated crop imaging applications. **Comput. Electron. Agric.**, v. 63, n. 2, p. 282–293, out. 2008.

MOGILI, U. M. R.; DEEPAK, B. B. V. L. Review on application of drone systems in precision agriculture. **Procedia Comput. Sci.**, v. 133, p. 502–509, jan. 2018.

MOURHIR, A. et al. Exploring precision farming scenarios using fuzzy cognitive maps. **Sustain. Sci. Pract. Policy**, Multidisciplinary Digital Publishing Institute, v. 9, n. 7, p. 1241, jul. 2017.

NARENDRA, V. G.; HAREESH, K. S. Prospects of computer vision automated grading and sorting systems in agricultural and food products for quality evaluation. **Int. J. Comput. Appl. Technol.**, Foundation of Computer Science, v. 1, n. 4, fev. 2010.

OLIVEIRA., A. **Assimetria e Curtose**. 2021. Disponível em <http://alexandreprofessor.blogspot.com/p/assimetria-e-curtose.html>. Acesso em 18 setembro 2021.

ONYANGO, C. M. et al. Precision agriculture for resource use efficiency in smallholder farming systems in Sub-Saharan africa: A systematic review. **Sustainability**, v. 13, 2021.

OTSU, N. A threshold selection method from gray-level histograms. **IEEE Transactions on Systems, Man, and Cybernetics**, v. 9, n. 1, p. 62–66, 1979.

PAUSTIAN, M.; THEUVSEN, L. Adoption of precision agriculture technologies by german crop farmers. **Precis. Agric.**, v. 18, n. 5, p. 701–716, out. 2017.

PURI, V.; NAYYAR, A.; RAJA, L. Agriculture drones: A modern breakthrough in precision agriculture. **J. Stat. Manage. Syst.**, Taylor & Francis, v. 20, n. 4, p. 507–518, jul. 2017.

RADON, J. On the determination of functions from their integral values along certain manifolds. **IEEE Transactions on Medical Imaging**, v. 5, n. 4, p. 170–176, 1986.

ROCHA, B. M. et al. Evaluation and detection of gaps in curved sugarcane planting lines in aerial images. In: **2020 IEEE Canadian Conference on Electrical and Computer Engineering (CCECE)**. [S.l.: s.n.], 2020. p. 1–4. ISSN 2576-7046.

SADEGHI, M.; BEHNIA, F.; AMIRI, R. Window selection of the savitzky–golay filters for signal recovery from noisy measurements. **IEEE Transactions on Instrumentation and Measurement**, v. 69, n. 8, p. 5418–5427, 2020.

SAVITZKY, A. A historic collaboration. **Analytical Chemistry**, v. 61, n. 15, p. 921A–923A, 1989. PMID: 22882064. Disponível em: <https://doi.org/10.1021/ac00190a744>.

SILVA, R. R. d. Detection of sugarcane crop rows from uav images using semantic segmentation and radon transform. **Universidade Federal de Uberlândia, Uberlândia**, 2020.

SOUZA, C. H. W. d. et al. Mapping skips in sugarcane fields using object-based analysis of unmanned aerial vehicle (UAV) images. **Comput. Electron. Agric.**, v. 143, p. 49–56, dez. 2017. ISSN 0168-1699.

SPEKKEN, M.; SALVI, J.; MOLIN, J. A method to evaluate paralelism for machine logged positions. In: . [S.l.: s.n.], 2014.

STURM, P. Panoramic camera. **Computer Vision**, 2014.

TARABA, P. **Optimal blending of multiple independent prediction models**. 2021.

TONINI, A. et al. Remote estimation of target height from unmanned aerial vehicle (UAV) images. **Remote Sensing**, Multidisciplinary Digital Publishing Institute, v. 12, n. 21, p. 3602, nov. 2020.

TSOUROS, D. C.; BIBI, S.; SARIGIANNIDIS, P. G. A review on UAV-Based applications for precision agriculture. **Information**, Multidisciplinary Digital Publishing Institute, v. 10, n. 11, p. 349, nov. 2019.

WANG, F.; WANG, X. Fast and robust modulation classification via kolmogorov-smirnov test. **IEEE Transactions on Communications**, v. 58, n. 8, p. 2324–2332, 2010.

Wikipedia contributors. **Kolmogorov–Smirnov test — Wikipedia, The Free Encyclopedia**. 2022. [Online; accessed 5-December-2022]. Disponível em: <https://en.wikipedia.org/w/index.php?title=Kolmogorov%E2%80%93Smirnov_test&oldid=1122144808>.

WOEBBECKE, D. M. et al. Color indices for weed identification under various soil, residue, and lighting conditions. **Trans. ASAE**, v. 38, n. 1, p. 259–269, 1995.

YANG, G. et al. Unmanned aerial vehicle remote sensing for Field-Based crop phenotyping: Current status and perspectives. **Front. Plant Sci.**, v. 8, p. 1111, jun. 2017.

YU, Y. et al. Crop row segmentation and detection in paddy fields based on Treble-Classification otsu and Double-Dimensional clustering method. **remote sensing**, v. 13, n. 5, fev. 2021.

ZAREIFOROUSH, H. et al. Potential applications of computer vision in quality inspection of rice: A review. **Food Engineering Reviews**, v. 7, n. 3, p. 321–345, set. 2015.

ZHANG, C.; KOVACS, J. M. The application of small unmanned aerial systems for precision agriculture: a review. **Precis. Agric.**, v. 13, n. 6, p. 693–712, dez. 2012.

ZHANG, X. et al. Automated robust crop-row detection in maize fields based on position clustering algorithm and shortest path method. **Comput. Electron. Agric.**, v. 154, p. 165–175, nov. 2018. ISSN 0168-1699.